

[Click here to view linked References](#)

A mapping approach for the investigation of Ti-OH relationships in metamorphic garnet

Julien Reynes¹, Pierre Lanari¹ and Jörg Hermann¹

¹: Institute of Geological Sciences, University of Bern, Baltzerstrasse 3, Bern, CH-3012 Switzerland

Abstract

Garnet is a nominally anhydrous mineral that can incorporate several hundreds of ppm H₂O in the form of OH groups, where H⁺ substitutes for cations in the garnet structure. In order to understand the effect of such small amounts of H₂O on the physical and chemical properties of garnet, it is essential to determine where and how the OH groups are incorporated into the mineral structure. We investigated correlations between major and minor element maps acquired with the electron probe micro-analyzer and H₂O maps measured with Fourier transform infrared spectroscopy coupled to a focal plane array detector at the microscale to determine possible coupled substitutions. A set of algorithms was developed to match the maps pixel by pixel. They allow the computation of the garnet structural formula taking the H₂O content into account and the calculation of correlations between H₂O and other elements on the basis of 10'000s of points. This new approach was applied to two hydrous garnet samples both showing H₂O and chemical zoning. The first sample consists of a grossular-rich garnet from a high-pressure metarodingite ranging from 200 to 900 ppm H₂O. The second sample contains a Ti-rich andradite garnet ranging from 200 to 8500 ppm H₂O. For the grossular-rich garnet, a 1:1 correlation between Ti and H has been observed suggesting that H occurs as tetrahedral (2H)²⁺ point defect, charge compensated by 2 Ti⁴⁺ on the octahedral site. Based on this, a new hydrous garnet endmember with the formula Ca₃Ti₂H₂Si₂O₁₂ is proposed. This 2Ti^{VI} ↔ (2H)^{IV} exchange mechanism is mainly responsible for the high amounts of TiO₂ (up to 11 wt%) in the investigated Ti-andradite. The incorporation of (2H)²⁺ instead of (4H)⁴⁺ on the tetrahedral site has important consequences for the normalisation of the garnet and hence on the determination of Fe²⁺/Fe³⁺ based on stoichiometry. In the garnet from the metarodingite a small scale zoning in H₂O contents of less than 100 μm can be resolved, indicating that the Ti-H defect is stable up to eclogite facies conditions and not modified by diffusion even at timescales of millions of years.

1
2
3 31 Keywords: Quantitative compositional mapping – Garnet – FTIR mapping –Nominally anhydrous
4
5 32 minerals
6
7

8 33

9
10 34 **Introduction**

11
12 35 Garnet is a common metamorphic mineral formed during prograde dehydration reactions such as
13
14 36 encountered during the subduction of oceanic crust and sediments. The garnet formula contains
15
16 37 neither H₂O nor OH groups, nevertheless it can incorporate several hundreds of ppm H₂O as OH
17
18 38 groups where H⁺ incorporation is charge-balanced by cation substitutions. Because of the large P-T
19
20 39 stability field of garnet, the incorporated H₂O can be transported inside the slab to the deep mantle and
21
22 40 might play an important role in the Earth's deep water cycle. It is essential to know where the OH
23
24 41 groups are located in the garnet structure, and which coupled substitutions exist for the incorporation
25
26 42 of H⁺. The dominant substitution found so far is the replacement of a Si⁴⁺ cation by 4H⁺, known as the
27
28 43 hydrogarnet point defect (Cohen-Addad et al. 1967; Foreman 1968; Lager et al. 1987). Other point
29
30 44 defects have been proposed, involving H⁺ substitutions for dodecahedral and octahedral cations
31
32 45 (Andrut et al. 2002; Basso et al. 1984; Geiger et al. 1991). Coupled substitutions have been invoked
33
34 46 such as H-B and H-Li point defects (Lu and Keppeler 1997) and even incomplete silicon vacancies,
35
36 47 like 3H⁺ substituting for a Si⁴⁺ and being compensated by Ti⁴⁺ in octahedral site (Khomenko et al.
37
38 48 1994), or Fe³⁺ or Fe²⁺ together with one of two H⁺ in the tetrahedral site in Ti-rich garnets (Kühberger
39
40 49 et al. 1989). Recent studies support that multiple point defects are present in single garnet grains
41
42 50 (Geiger and Rossman 2018; Reynes, et al. 2018). It has been shown that garnet composition does
43
44 51 influence the incorporation of OH groups in the garnet structure. Garnet is a complex solid solution
45
46 52 involving various endmembers. Spessartine (Mn-Al), almandine (Fe²⁺-Al), pyrope (Mg-Al) constitute
47
48 53 the widespread pyralspite subfamily, whereas grossular (Ca-Al), andradite (Ca-Fe³⁺) and uvarovite
49
50 54 (Ca-Cr³⁺) belong to the ugrandite subfamily. Garnet dominated by ugrandite endmembers can
51
52 55 incorporate up to several wt.% H₂O (Rossman and Aines 1991), whereas pyralspite garnets usually
53
54 56 incorporate only a few hundreds of ppm (Aines and Rossman 1984a). Spessartine can incorporate
55
56
57
58
59
60
61
62
63
64
65

57 more water (up to 1000 ppm H₂O, Arredondo et al. 2001) than pyrope and almandine (< 150 ppm
58 H₂O). Because garnet has these various solid solutions and their affinity for H₂O seems to differ, a
59 correlation between major elements and OH groups at a comparable scale is needed. Major and minor
60 element chemistry of garnet is usually measured by Electron Probe Micro-Analysis (EPMA), which
61 allows mapping with a resolution up to 1 μm. Fourier Transform Infrared spectroscopy (FTIR) is the
62 optimal analytical technique to measure OH groups in garnet. This method has various advantages: 1)
63 high resolution (down to ~ 5 μm with appropriate objective and detector); 2) low limit of detection
64 (~1 ppm H₂O); 3) the wave number of absorption bands is specific to the environment where H⁺ is
65 located: the band positions vary with the nearest neighbours of the vibrating OH group and is then
66 influenced by local charge balance; 4) it is relatively cheap and fast. Therefore, the challenge to
67 investigate H⁺ substitution in garnet is to match compositional maps obtained with these two different
68 analytical techniques.

69 This study presents a novel approach and a set of programs for stacking H₂O maps acquired by FTIR
70 with quantitative compositional maps obtained by EPMA. This allows matching pixel by pixel of the
71 two maps, providing a database of 10⁷000s to 100⁷000 individual points that can be statistically
72 assessed in order to determine coupled substitutions involving H⁺ in garnet. Advanced processing of
73 the FTIR data using deconvolution of the spectra provides additional information of the structural
74 position of OH groups in the garnet structure. This technique was applied to a grossular-rich garnet
75 from a metarodingite from Servette (Aosta valley, Italy), and a Ti-rich andradite from a
76 metapyroxenite layer in ultramafic rocks from Valmalenco (Italy). In both cases, a strong correlation
77 between the minor element Ti and H₂O contents was found and a new hydrous garnet endmember
78 with the formula Ca₃Ti₂H₂Si₂O₁₂ is proposed. The influence of H substitution on the computation of
79 Fe²⁺/Fe³⁺ ratios in garnet, which can be used as a redox indicator, is also assessed.

81 **Samples and techniques**

82 *Sample description*

83 The two samples presented in this work were collected in the Alps. The first sample *ServRod* is a
84 garnet from a rodingite from the Servette area (St Marcel, Aosta valley, Italy). The various rock types
85 in this area are interpreted as both oceanic and continental margin units derived from the Mesozoic
86 Tethyan ocean and the Palaeozoic crust of the African margin (Tartarotti et al. 2017). The area of St.
87 Marcel is known for metabasalts hosting a Fe-Cu sulphide deposit and a Mn-ore deposit (Praz Borna),
88 both related to oceanic hydrothermal processes. The mafic-ultramafic rock suite experienced extensive
89 oceanic metasomatism, followed by high-pressure metamorphism during the Alpine subduction with
90 peak metamorphism at 550 ± 60 °C and 2.1 ± 0.3 GPa (Martin, et al. 2008). These conditions were
91 derived from talc-schists that are associated with serpentinites. Within the same serpentinites, meta-
92 rodingite occurs as meter-sized boudins that are interpreted to derive from mafic dykes that
93 experienced rodingitisation during the seafloor alteration. The close link between the talc-schists,
94 serpentinites and meta-rodingites suggest that all rock types share a common metamorphic evolution.
95 The meta-rodingites are composed of 60% brownish garnet and 40% green diopside. Garnet grains are
96 1-3 mm in diameter, rock forming, automorphic with no evidence of resorption. No low-pressure
97 hydrous mineral associated to retrogression was observed in the sample (see supplementary Figure S1
98 for optical image).

99 The second sample *TiAnd* was collected in Valmalenco, Italy. It consists of 5-10 millimetre sized
100 garnet crystals in a metapyroxenite layer identified as melanite (Ti-rich andradite). Details about this
101 sample were previously published by Müntener and Hermann (1994). Garnet formed in equilibrium
102 with diopside, chlorite and minor ilmenite, perovskite and magnetite and is thought to have
103 crystallised at low pressures of 0.5 ± 0.2 GPa and a maximum temperature of 400-450° C. The garnet
104 grains are optically zoned, with a black melanite core surrounded by a large yellow-brownish
105 andradite rim (see supplementary Figure S1 for optical image).

106 The garnets were cut near the centre of each grain. Both samples were prepared as double polished
107 thick sections on a glass slide (280 µm for *ServRod* and 162 µm for *TiAnd*). This thickness was
108 selected in order to get 1) good optical transmission and 2) a low H₂O detection limit with infrared
109 spectroscopy. Electron microprobe X-ray mapping was performed first, before transmission infrared

110 spectroscopy, which requires detaching the thick sections from the glass. The two techniques have
111 different excitation volumes, as one is a near-surface analysis (EPMA) and the other a transmission
112 technique (FTIR). This point is discussed in details below.

113

114 *Analytical techniques*

115 Electron microprobe (EPMA)

116 Major elements maps of garnet were acquired using a JEOL JXA 8200 superprobe instrument at the
117 Institute of Geological Sciences, University of Bern. Thick sections were polished to $\frac{1}{4}$ μm and
118 carbon coated. The accelerating voltage was set to 15 keV and the beam current to 100 nA for
119 mapping and 20 nA for conventional spot analyses. A set of spot analyses was also acquired in the
120 mapped area for calibration. The following elements were measured: Si, Ti, Al, Cr, V, Fe, Mn, Mg
121 and Ca and calibrated using a set of natural and synthetic standards: almandine (SiO_2 , Al_2O_3 , FeO);
122 anorthite (CaO); ilmenite (TiO_2); tephroite (MnO); olivine (MgO); spinel (Cr_2O_3); shcherbinaite
123 (V_2O_3). Peak and background were measured for 20 s and 2×10 s, respectively for spot analyses and
124 a dwell time of 150 ms was used for mapping. Two maps were acquired: a map of 1000x1000 pixels
125 with a step size of 2 μm on the ServRod sample and a map of 650x650 pixels with a step size of 8 μm
126 for TiAnd. The maps were calibrated and further analysed using XMAPTOOLS 3.2.1 (Lanari et al.
127 2014, 2019). No time-related intensity drift was observed using the monitoring tools available in
128 XMAPTOOLS (see discussion and examples in Lanari et al. (2019)).

129

130 Fourier transform infrared spectroscopy (FTIR)

131 FTIR utilises vibration of OH groups when exposed to specific wavelengths of radiation. A specific
132 region of the mid-infrared, approximately $3000\text{-}3800\text{ cm}^{-1}$, typically corresponds to the stretching
133 frequency of OH groups in silicates. Measured absorbance enables quantification of the OH content in
134 the sample. This content is determined using the Beer-Lambert law with specific absorption

135 coefficients and is commonly expressed as H₂O ppm by weight (µg/g). FTIR also provides
136 information on the structural environment of these OH groups.

137 Transmission FTIR spectroscopy maps were acquired at the University of Bern. The instrument is
138 equipped with a Plexiglas chamber with controlled airflow and moisture to limit environmental
139 variations of CO₂ and H₂O (relative humidity < 10%). This instrument has two detectors: a single
140 spot, nitrogen-cooled mercury cadmium telluride (MCT) detector and a focal plane array (FPA)
141 detector –composed of 64 × 64 = 4096 liquid nitrogen-cooled MCT elements on a square array. The
142 minimum pixel size is 2.7 µm × 2.7µm. A 2x2 to 8x8 binning was used blowing up the pixel size to
143 respectively 5.4 × 5.4 µm and 21.6 × 21.6 µm, but improving the quality of each spectrum. The
144 choice of binning was also motivated by the size of the area measured, as the Bruker® OPUS®
145 program cannot acquire maps containing more than 200 000 spectra. Garnet from Servette Rodingite
146 was measured with a binning by 2 of the FPA detector and a pixel size of 5.4 µm. The map represents
147 14 × 14 tiles of 172.8 µm with 1024 spectra per tile – leading to 200.704 spectra in total. 140 scans
148 per spectrum were chosen in order to complete the map in less than 5 hours – the maximum autonomy
149 of cooling of the FPA detector. For the second sample TiAnd, a map of 35 × 35 tiles and a binning of
150 8 was set – leading to a pixel size of 21.6 µm – 78.400 spectra, and 10 scans per spectrum. The
151 relatively low number of scans was required to maintain the measurement time below 5 hours. The
152 data quality is still good as the binning of the detector improves the signal to noise ratio. Each
153 spectrum was acquired in the middle infrared between 900 and 4000 cm⁻¹ with 8 cm⁻¹ wavenumber
154 resolution. Spectra were baseline corrected using the concave rubberband algorithm of OPUS® with
155 64 points and four iterations. For TiAnd, pseudo-transmission measurements were acquired using an
156 ATR objective coupled with the single spot MCT detector. The objective is composed of a
157 germanium crystal touching the sample, resulting in an evanescent wave of infrared light that is
158 transmitted through the uppermost portion of the sample, allowing measurement of a very thin layer at
159 the surface of the sample, with a penetration of less than 1 µm and a spot size around 30 µm (see
160 supplementary material S2 for details). This method allows high water contents, up to several wt.%

161 of water to be measured but it does not detect low water content < 1000 ppm H₂O because of the
162 small penetration depth.

163 *Data processing*

164 OPUS and *FPAMap*

165 OPUS[®], the main Bruker[®] FTIR program, was used for data visualisation, baseline subtraction and,
166 where needed, atmospheric H₂O compensation. An in-house program *FPAMap* was developed as a
167 MATLAB[®]-based graphical user interface (GUI) for advanced data processing. It reads the integrated
168 areas determined by OPUS from the OH stretching region and overtone. In the case of garnet, the OH
169 stretching region results in absorbance at 3400 - 3800 cm⁻¹ and the overtone region – associated to
170 harmonics of Si-O bonds vibrations – produces absorption bands at 1600 - 2000 cm⁻¹. For the sample
171 ServRod, an overtone-thickness relationship was applied to correct for small variations in the
172 thickness of the sample (thickness = 1.2786 * overtone, see Reynes et al. (2018)). The absorption map
173 for water is then normalised to 1 cm thickness of garnet. The H₂O content (in µg/g H₂O) is computed,
174 using an appropriate absorption coefficient k_{abs} defined by equation (1)

$$k_{abs} = \frac{c \times M_{H_2O}}{d \times \varepsilon} \quad (1)$$

176 Where c is a normalisation constant equal to 10⁶ (corresponding to the conversion from g/g to µg/g
177 (ppm H₂O), M_{H_2O} is the molar mass of H₂O, d is the density of the mineral and ε the extinction
178 coefficient, a.k.a calibration coefficient – determined by an independent method and specific to a
179 mineral. The coefficient from Maldener et al. (2003) for grossular, $\varepsilon = 14400 \text{ l.mol}^{-1}.\text{cm}^{-2}$ was
180 chosen, where a H₂O content of 870 ppm was derived by nuclear reaction analysis (NRA) on a
181 grossular crystal. A complementary study by Reynes et al. (2018) has shown that this coefficient is
182 suitable for grossular-rich garnet.

183

184 In the case of the TiAnd sample, a thickness correction based on overtone was not possible because of
185 compositional variability affecting the overtone region shape and absorption and thus a constant

186 thickness of 162 μm , measured with a Mitutoyo® micrometer, was used. The overtone map was only
187 used to detect mineral inclusions. The same extinction coefficient ε was used (see below for
188 justification). The output file of *FPAMap* contains a H_2O content map of the sample, expressed in
189 ppm H_2O .

191 *StackMaps*

192 A second GUI-based program, *StackMaps*, was designed for the superposition of FTIR and EPMA
193 maps. As the two datasets were obtained on two different instruments, and the sections were detached
194 from the glass to be measured by transmission on FTIR, it was impossible to analyse the same area
195 with the same resolution and orientation. The FTIR map was acquired on a larger zone, and a
196 geometric transformation based on a set of reference points (crystal edges, cracks, inclusions) is
197 needed to find the correct position relative to the EPMA maps via affine transformation, combining
198 translation, scaling, shearing and rotation. As the pixel size is different, the map with the lowest
199 resolution (FTIR) was resampled based on the highest resolution (EPMA). The output of *StackMaps*
200 is a H_2O map with the same orientation and resolution than the EPMA map. The major element
201 composition of each pixel is known as well as the corresponding H_2O content allowing a structural
202 formula to be calculated. This correction is required as the FTIR map can be distorted, due to lower
203 accuracy of the stage and binning, in comparison to microprobe map.

204 This program has been incorporated as an add-on in the mapping package XMAPTOOLS (Lanari et al.
205 2014, 2019).

207 *GarnetH2O*

208 The third program *GarnetH2O* is an external function of XMAPTOOLS for generating maps of
209 structural formula of garnet based on the maps of SiO_2 , TiO_2 , Al_2O_3 , Cr_2O_3 , V_2O_3 , FeO , MnO , MgO ,
210 CaO and H_2O expressed in mass weight percentage of oxide. Normalisation is done on a basis of 8
211 cations, with the possibility of counting $(2\text{H})^{2+}$ or $(4\text{H})^{4+}$ as one cation, as they do substitute for one

1
2 212 silicon. For this study, there is good evidence that H is incorporated in the garnet as $(2\text{H})^{2+}$. Therefore
3 213 garnet normalisation assumes all H as $(2\text{H})^{2+}$ and a fixed cation number of 8. The proportion of Fe^{2+}
4 214 and Fe^{3+} is then adjusted assuming a sum of charges of 24 (see supplementary material S3). The
5 215 tetrahedral site is considered as being occupied by Si^{4+} , Hx ($(2\text{H})^{2+}$ or $(4\text{H})^{4+}$) and potentially Al^{3+} ,
6 216 octahedral site by Ti^{4+} , Al^{3+} , V^{3+} , Cr^{3+} , Fe^{3+} and in the case of Ti-rich Andradite garnets Fe^{2+} and Mg^{2+}
7 217 and Mn^{2+} . The dodecahedral site has Ca^{2+} , Mn^{2+} , Mg^{2+} and Fe^{2+} , only Ca^{2+} and Mn^{2+} for Ti-rich
8 218 andradite.
9
10
11
12
13
14
15

16 219

19 220 *Deconvolution and correction of artefacts*

22 221 A deconvolution was applied to the spectra of both maps to better resolve the water region and define
23 222 the relative contributions of each peak. The code, written in MATLAB[®], uses a modified version of
24 223 the *peakfit* function developed by Tom O’Haver (O’Haver 2015). The position of the different peaks
25 224 is fixed, and the program only adjusts the peak heights and widths to fit the measured signal. Results
26 225 consist of height, width and area data for each peak, which can be displayed as maps as well. The
27 226 same resampling algorithm and geometric transformations were applied as previously described for
28 227 the FTIR water map.

29 228 For the sample ServRod, fluid inclusions caused a broad absorption band centred at 3420 cm^{-1} . A
30 229 specific algorithm was used in order to model fluid inclusion by fitting this region with a broad
31 230 Gaussian centred on 3420 cm^{-1} – and minimising the residual area between 3400 and 3100 cm^{-1} . This
32 231 procedure was applied to each spectrum and resulted in a map of fluid inclusion density. The spectra
33 232 were corrected for fluid inclusion. Only the garnet OH stretching group bands are discussed in the
34 233 following.
35
36
37
38
39
40
41
42
43
44
45
46
47
48
49
50
51

52 234

54 235 **Results**

57 236 *EPMA maps*

58
59
60
61
62
63
64
65

237 Compositional maps obtained by EPMA are presented on Fig. 1 for ServRod and Fig. 2 for TiAnd

238 (additional compositional maps are presented in supplementary material S4). These maps are

239 expressed in atoms per formula units (apfu), calculated on a 8 cations basis.

240 ServRod garnet shows a high Ca (>2.6 apfu) and Al content (>1.7 apfu). Therefore, it is a grossular

241 garnet with minor andradite and almandine component (see Table 1 for endmember formula). Various

242 oscillatory zonings in dodecahedral cations such as Ca^{2+} , Fe^{2+} and Mn^{2+} as well as octahedral cations

243 Al^{3+} , Ti^{4+} and Fe^{3+} - create complex but sharp zoning patterns. The Ti content increases from the rim

244 to core by a factor of five, varying from 0.01 to 0.05 apfu.

245 TiAnd garnet is mainly characterised by three chemical zones, delimited by their Ti content (Fig. 2).

246 The rim zone, with $\text{Ti} < 0.2$ apfu shows a high $\text{Fe}^{3+} = 2$ apfu and a $\text{Si}^{4+} = 3$ and dodecahedral site fully

247 occupied by Ca^{2+} - characteristic of andradite garnet. Small and sharp bands appear in the Ti map,

248 with Ti rising from 0.1 to 0.25 apfu. The second zone is only 200 μm wide and consists of a sharp

249 increase of Ti from 0.2 to 0.4 apfu. The core zone is characterised by a high Ti content up to 0.7 apfu

250 and a Si deficiency ($2.7 < \text{Si} < 3$). The Mg content is increasing from rim (0.02) to core (0.08 apfu). The

251 Ca pattern does not vary with the zones with a value around 3 apfu and thus Fe^{2+} and Mg^{2+} occupy

252 octahedral sites. As a consequence, zoning involves only variations in octahedral and silicon site

253 occupancies.

254 *FTIR single spectra*

256 Core to rim spectra were extracted for both samples and are shown in Fig. 3. Servette rodingite

257 spectra (ServRod, see Fig. 3a) display three bands at 3500 to 3700 cm^{-1} . A main band, around 3595

258 cm^{-1} is flanked by two smaller bands on either side at around 3546 cm^{-1} and 3652 cm^{-1} of similar

259 intensity. These bands are visible in all analyses from core to rim. According to peak positions and

260 shapes, this sample is similar to class 5 grossular according to classification of Rossman and Aines

261 (1991) (rodingite, Liguria), despite the singularity that the main band is at lower wave number than in

262 the classification (3595 cm^{-1} for 3612 cm^{-1}). The spectra in the core region are affected by a large

263 bump due to fluid inclusion, centred on 3420 cm^{-1} . The overtone region, 1600-2000 cm^{-1} shows the

264 characteristic peak and shoulder of garnet, and allows the sample thickness to be determined (see
1 above).
2
3
4 266 Titanium andradite (TiAnd) spectra show absorption in the range 3500-3700 cm^{-1} (Fig. 3b) similar to
5
6
7 267 the Servette rodingite. Spectra corresponding to the rim zone, optically yellow-brownish, display two
8
9 268 well-defined bands at 3563 and 3604 cm^{-1} , characteristic of pure andradite (Amthauer and Rossman
10
11 269 1998). Darker zones show a stronger absorption of the first band, around 3563 cm^{-1} and the
12
13 270 appearance of a second band, around 3581 cm^{-1} , which forms a doublet with the previous. The core of
14
15 271 the sample completely absorbs IR radiation between 3530 and 3640 cm^{-1} due to the high water content
16
17 272 (> 5000 ppm H_2O). The overtone region 1600-2000 cm^{-1} shows variability between the rim
18
19 273 characterized by sharp bands and the core zone with smoother peaks. The absorbance of these bands
20
21 274 is modified up to 50 %, though the thickness is not varying by more than 5%. These differences imply
22
23 275 that a linear overtone to thickness law is not appropriated for this sample.
24
25
26

276 *FTIR maps*

277 The H_2O distribution maps of the two garnets (Fig. 4a, c) display surprisingly sharp, regular zoning
28
29
30 278 patterns. The comparison of the H_2O zoning with the major and minor element zoning (Figs. 1, 2)
31
32 279 provides further evidence for a strong correlation between Ti and H_2O . The map correlation algorithm
33
34 280 *StackMaps* was used to superimpose H_2O with EPMA maps. Fig. 4 shows for each sample the maps
35
36 281 of H_2O and TiO_2 with the corrected resolution and orientation. ServRod maps, (Fig. 4a-b) show
37
38 282 oscillatory zoning in TiO_2 and H_2O . The H_2O content is increasing from 300 ppm H_2O at the edge of
39
40 283 the crystal to 900 ppm H_2O in the interior, while TiO_2 increases in a similar pattern from 0.2 to 0.9
41
42 284 wt%. The noisy zone present on the top left corner of the water map is an artefact linked to the smaller
43
44 285 size of the analysed grain. TiAnd (Fig. 4c and 4d.) reveals one order of magnitude higher TiO_2 , from
45
46 286 the rim below 1 wt.% up to 10 wt.% in the core. Similarly the H_2O content ranges from 300 ppm to
47
48 287 5000 ppm inward. As shown in Figure 3, the H_2O content in the core of the sample is underestimated
49
50 288 due to the nearly complete absorption of the infrared light.
51
52
53
54
55

56 289

59 290 *ATR profile*

60
61
62
63
64
65

291 To deal with complete absorption issues in the core of TiAnd, a rim-core profile was measured on the
292 same grain with the ATR objective, using a spectral resolution of 8 cm⁻¹, 512 scans and a step size of
293 45 μm. The profile is presented on Fig. 5, and is located on Fig. 4 – it follows the FPA profile
294 presented on Fig. 3b. On Fig. 5a, the integrated absorption between 3400 and 3700 cm⁻¹ is displayed
295 together with the integrated absorption measured with the FPA detector. Distinct features noticed on
296 the two profiles (purple dots) enable to calibrate the ATR spectra for H₂O content and compute the
297 effective penetration depth of the IR beam in the range 3500-3700 cm⁻¹ which is 0.56 μm (details in
298 supplementary material S5). While the FPA profile reaches complete absorption and a flat trend of
299 H₂O content towards the core at about 5000 ppm H₂O, the ATR profile reveals a higher content up to
300 8000 ppm H₂O. Using the ATR profile (Fig. 5), an average H₂O content of 6100 ppm in the core can
301 be recalculated, assuming a spheric approximation of the garnet. This is in excellent agreement with
302 the 6600±1000 ppm H₂O obtained for separated garnet cores measured for the bulk water content by
303 thermal combustion measurements (Müntener and Hermann 1994). This underlines that the
304 coefficient chosen for calibration of the IR spectra, 14400 l.mol⁻¹.cm⁻² (Maldener et al. 2003) for a
305 grossular garnet is also appropriate for Ti-rich andradite. Detection limits appear to be in the region of
306 500 ppm H₂O, which is impressive considering that the depth of penetration is below 1 μm with the
307 ATR objective.

309 *Correlation maps and correlation plots*

310 For both samples, H₂O and TiO₂ contents are increasing from rim to core (Fig. 4). In order to test
311 coupled substitutions, the molar abundance is required to quantify by how many moles H increases
312 with one mole of Ti.

313 The notation n*x corresponds to the number of moles of x within one tonne of mineral.

314 n*H is computed using:

$$315 \quad n^*H = H_2O(ppm) \times \frac{2}{M_{H_2O}} \quad (2)$$

316 with H₂O in ppm and M_{H₂O} the molar mass of H₂O (18.015 g.mol⁻¹). Similarly, n*Ti is obtained using:

317
$$n^*Ti = TiO_2(wt. \%) \times \frac{1}{M_{TiO_2}} \times 10\,000 \quad (3)$$

318 with TiO_2 wt.% and M_{TiO_2} the molar mass of TiO_2 (79.866 g.mol⁻¹). Two rectangular areas free of
319 artefacts and representative of the variations were selected for further investigation. The results are
320 presented in Figure 6 containing 100 000 pixels for the ServRod and 110 000 pixels for the TiAnd
321 maps. The value of n^*Ti for each pixel was plotted in a binary diagram against the corresponding n^*H
322 for both samples and the results presented as density maps (Fig 6c-d). Each pixel colour is
323 proportional to the number of analyses (i.e. originally pixels of the maps shown in Fig 6a-b)
324 overlapping the pixel using a logarithmic scale. For ServRod, the yellow zones on density maps
325 correspond to density above 50 analyses, and represent the main compositional groups in the crystal.
326 This dataset was classified into five compositional groups (Fig. 6e). The linear fit between Ti and H
327 has a slope of 0.96 over all five zones (Fig 6c). In the case of the TiAnd sample (Fig. 6d), the
328 relationship between n^*Ti and n^*H was investigated separately in three regions of compositions (Fig.
329 6f) corresponding to (1) the low-Ti rim, (2) the intermediate mantle and (3) the core enriched in Ti.
330 For n^*H ranging between 0 to 200 moles/t, the linear regression has a slope of 1.28. The slope
331 changes to 1.89 for the region with n^*H comprised between 200 and 370 moles/t. Over 370 moles/t,
332 water measurement by transmission is not reliable because of nearly complete absorption. Therefore,
333 for $n^*H > 370$ moles/t, only single points extracted from the ATR profile presented on Figure 5 are
334 plotted, and the regression gives a slope of 1.16.

335

336 *Structural formula and substitution mechanism*

337 The full quantification of garnet composition involving also water provides the basis for the
338 calculation of the structural formula. Selected EPMA data of ServRod are presented in Table 2 and
339 TiAnd on Table 3. In ServRod, there is a slight decrease of Si (in apfu) from rim to the core with a
340 concomitant increase in 2H. Only in the core, a small amount of Al is required to fill the tetrahedral
341 site. The excellent correlation of H to Ti (Fig. 6c) is also noted in the structural formula with twice as
342 much Ti than 2H. This suggests that the coupled substitution of 2H on the Si site is charge balanced

343 by 2Ti on the octahedral site. There is not enough Al and Ti to fully occupy the octahedral site and
344 thus a small amount of Fe³⁺ is required. The dodecahedral site is dominantly filled with Ca with minor
345 Fe²⁺, and Mn and traces of Mg.

346 TiAnd has the dodecahedral site filled almost completely by Ca²⁺. Thus Fe²⁺ and Mg²⁺ substitute into
347 the octahedral site in the core of the garnet, providing evidence for the Morimotoite substitution
348 occurring in Ti-rich andradite garnet $2Fe^{3+} \leftrightarrow Ti^{4+} + Fe^{2+}$ (see Table 1 for endmember definition).
349 The core is Si deficient with 0.3 to 0.4 apfu missing, compensated mainly by (2H)²⁺ giving raise to the
350 coupled substitution $2Fe^{3+} + Si^{4+} \leftrightarrow 2Ti^{4+} + (2H)^{2+}$. This substitution is responsible for 2/3 of
351 the Ti incorporation in the andradite. Some minor Al³⁺ is needed in the high Ti-andradite following
352 another Ti substitution mechanism, called schorlomite $Fe^{3+} + Si^{4+} \leftrightarrow Ti^{4+} + Fe^{3+}$. Results of
353 structural formula computation from X-ray chemical map and FTIR water maps are presented on
354 Figure 1 for ServRod and Figure 2 for TiAnd, and take into account the H₂O content measured by
355 FTIR, with H counting has (2H)²⁺ cation occupying the silicon site. For ServRod sample (Fig.1) the
356 (2H) apfu map is equivalent to 1/2 times the Ti apfu map.

357

358 *Deconvolution of spectra*

359 The integrated absorbance permits calculation of total H₂O in the garnet structure but it does not take
360 into account that several peaks/bands may exist for a sample, and that their positions and relative
361 intensities may vary. However, FTIR spectra also contain detailed information regarding the
362 environment of the OH groups in the garnet structure that can be extracted using spectrum
363 deconvolution. The deconvolution consisted in fitting each measured spectrum with Lorentzian or
364 Gaussian peaks in order to resolve the different band contribution. Four parameters were obtained for
365 each peak: position, width (half-width – the width of the distribution at height divided by two), height
366 and area. Selected spectra were extracted from the maps and are presented on Fig. 7 for ServRod and
367 Fig. 8 for TiAnd. Gaussian peaks were used for the sample ServRod and Lorentzian peaks for TiAnd
368 in order to obtain the best deconvolution possible for each case. Four representative spectra (see Fig.
369 4a for location) were selected for ServRod, and are plotted in Figure 7. Spectra can be resolved by at

1
2
3
4
5
6
7
8
9
10
11
12
13
14
15
16
17
18
19
20
21
22
23
24
25
26
370 least 3 peaks, after a correction of the signal to remove a broad Gaussian peak centred at 3420 cm⁻¹
371 caused by fluid inclusions. The first peak around 3547 cm⁻¹ does not show a strong protuberance and
372 is most of the time limited to a shoulder, due to its proximity with the main peak. It always appears as
373 the second peak in term of intensity and area. The main peak around 3595 cm⁻¹ and the third peak
374 around 3652 cm⁻¹ both show distinct local maxima. The fluid inclusion peak is apparently decoupled
375 from the estimated water content – even if the core of the garnet shows the highest water content and
376 is often associated with a large fluid inclusion peak. Selected deconvoluted spectra of sample TiAnd
377 (see Fig. 4c for location) are presented on Fig. 8. Deconvolution was performed using 4 Lorentzian
378 peaks with fixed positions at 3563, 3581, 3604 and 3624 cm⁻¹ for the spectra from FPA map. The
379 spectra acquired in the core of the sample with ATR objective allowed us to detect a fifth peak –
380 which appears as a shoulder at low wave number, around 3540 cm⁻¹. The main doublet is composed of
381 peak 3563 and 3581 cm⁻¹.

382 *Maps of deconvoluted peaks*

27
28
29
30
31
32
33
34
35
36
37
38
39
40
41
42
43
44
45
46
47
48
49
50
51
52
53
54
55
56
57
58
59
60
61
62
63
64
65
383 An automated process was developed which enables to process the entire maps made of tens of
384 thousands spectra. For ServRod, Parameter maps were produced and are displayed on Fig. 9. The
385 positions of peak 2 (3595 cm⁻¹) and peak 3 (3652 cm⁻¹) are varying across the map in a systematic
386 manner while this was not observed for peak 1 (map is available in supplementary material S6).
387 Comparing with compositional maps, it appears that the main peak 3592-3599 cm⁻¹ is following the
388 calcium content (Fig. 1d). Even if H is in tetrahedral site, Ca can influence the frequency of stretching
389 of the nearby OH bonds, though its direct influence on water incorporation is not obvious. Peak 3
390 (Fig. 9b) shows two main zones with a marked shift of the peak from 3646 in the core to 3654 cm⁻¹ at
391 the rim that is not related to any obvious change in garnet composition. Figure 9c represents the main
392 peak area map expressed in ppm H₂O using the equation 1 (area maps for peak 1 and 3 are shown in
393 supplementary material S7). Figure 9d is a map of the area of the fluid inclusions modelled peak,
394 expressed in cm⁻² corrected by the thickness of the sample. It does not provide quantitative
395 information about water content in fluid inclusions, as it is an integrated signal through the sample
396 thickness. It only shows a pseudo-density map depending on the localisation of the fluid inclusions

397 across the sample. This map shows that changes in OH band position and intensity are independent of
1
2 398 the H₂O band subtraction. The absence of relationship between structural OH and the amount of fluid
3
4 399 inclusions containing free H₂O demonstrates that the fluid inclusion correction applied to the FTIR
5
6 400 spectra is robust.

8
9 401 Deconvolution maps (location shown on Figure 4c-d) of a small area of sample TiAnd of the 4 main
10
11 402 peaks observed on FPA spectra were calculated, and compared to X-ray maps of Ti, Fe³⁺ and Al,
12
13 403 expected to be cations occupying the octahedral site (Fig. 10 and supplementary material S8).
14
15 404 Although the peak positions do not vary significantly across the map, the relative intensities (and
16
17 405 area) of each peak are varying. The two major peaks, 3563 cm⁻¹ and 3581 cm⁻¹ (Fig. 10a, b) are
18
19 406 correlated with the Ti content (Fig. 10c) with a 1/1 ratio (Fig. 10d), supporting the hypothesis that Ti
20
21 407 is directly influencing water incorporation in point defects related to the OH groups vibrating at these
22
23 408 wavenumbers. The peaks 3604 cm⁻¹ and 3624 cm⁻¹ (Supplementary material S8) appear to be
24
25 409 correlated with the Al content, though they contain less than 10 % of the total water quantified.
26
27
28
29
30

410

411 **Discussion**

412 *Spatial resolution and limitations of the mapping approach*

37
38 413 The resolution of the EPMA is dependent on the excitation volume of the electron beam and is
39
40 414 typically about 1-2 μm for the mapping conditions used in this study. The maximum resolution of the
41
42 415 FTIR is related to the wavelength of infrared light from 3-2.7 μm in the 3300-3700 cm⁻¹ absorption
43
44 416 region of OH in garnet. The minimum resolution of a single tile in the FPA detector images an area of
45
46 417 2.7 x 2.7 μm. We applied a 2x2 binning for the ServRod and a 8x8 binning for the TiAnd resulting in
47
48 418 a maximum resolution of 5.4 and 21.6 μm. The main limitation of the combination of maps presented
49
50 419 here is related to the correlation between near-surface analyses (EPMA) and transmission analyses
51
52 420 (FTIR). The different zones might be slightly inclined, leading to a smearing out of the signal. We
53
54 421 have shown that Ti and H are directly correlated in the ServRod (Fig. 4) and thus the comparison
55
56 422 between the EMPA Ti map and the FTIR H₂O map can be used to assess the resolution for this 270
57
58 423 μm thick sample. The features at the 100 μm scale are all easily resolved and visible on both maps.
59
60
61
62
63
64
65

1
2
3
4
5
6
7
8
9
10
11
12
13
14
15
16
17
18
19
20
21
22
23
24
25
26
27
28
29
30
31
32
33
34
35
36
37
38
39
40
41
42
43
44
45
46
47
48
49
50
51
52
53
54
55
56
57
58
59
60
61
62
63
64
65

424 The smallest features seen in the EPMA map are at the scale of 10 μm and these are not resolved with
425 the FTIR map. However in the detailed maps (Fig. 6a, b) and deconvoluted peak map of Fig. 9c
426 features of 30 μm are resolved, in agreement with the study of Jollands et al. (2019). This is further
427 confirmed by the comparison of the Ti map (Fig. 10c) with the map of the 3581 cm^{-1} peak in TiAnd
428 (Fig. 10b,d).

429 We recommend that the grain diameter should be at least 10 times bigger than the thickness of the
430 measured section and that the section is made near its centre. If the grain is too thin compared to the
431 thickness of the rock section, it will produce mixed FTIR spectra, which leads to noise in the FTIR
432 map as seen on the upper left corner of the ServRod sample (Fig. 4). A 10 times bigger grain diameter
433 ensures that growth zoning is nearly perpendicular to the surface (considering a rounded
434 approximation as shape of the grain, cut in its centre).

435 Other issues compromising the FTIR map are mineral or fluid inclusions and cracks. Fluid inclusions
436 can be filtered by spectra deconvolution (Fig. 9d). The effect of mineral inclusion depends on the type
437 of inclusion and on the ratio of the inclusion diameter versus the thickness of the mineral section
438 measured. Usually, the inclusions show an overtone region – or harmonics of Si-O bonds vibrations -
439 in the middle infrared between 1400-2200 cm^{-1} specific of the mineral type. As garnet shows
440 characteristic peaks in the overtone range 1600-2000 cm^{-1} , the possible effects of mineral inclusion
441 can be detected. The use of overtone-thickness correction when possible or thresholds on the overtone
442 help to remove the largest inclusions (e.g. Fig. 4c and d). It remains that small inclusions near the
443 surface (Fig. 4d) will not be visible in the water map. By contrast, some inclusions are visible in the
444 water map but not in the EPMA maps – see white zones on Fig. 4c and 4d. The cracks may cause
445 dispersion of the IR light, and might be partially filled with alteration products or even contaminated
446 by organic products due to the polishing (epoxy, glue, diamond paste solvent). Geometric and
447 oriented features are easily identified as artefacts.

448 The detection limit of transmission FTIR is linked to the sample thickness. Small grains with very low
449 water contents may not be measurable because of the limited thickness. The opposite is also true, a
450 sample with very high water content cannot be measured by transmission because even thin enough

451 sections would result in complete absorption. This is the case for the core of our TiAnd sample.

452 Considering these constraints, ideal is a grain of 1-3 mm in diameter, prepared in a section of 100-300

453 μm (a first guess on water content helps to select the appropriate thickness), which enables

454 quantitative mapping on the range 5-3000 ppm H_2O .

455

456 *Titanium- H_2O relationships: a new hydrous garnet endmember?*

457 Correlation of Ti and H was already observed in grossular-andradite garnet from Skarns by Johnson

458 (2003), but profiles were measured with a square beam of $100 \times 100 \mu\text{m}$ for FTIR and $10 \mu\text{m}$ beam for

459 EPMA. The mapping with a FPA detector enables a pixel size of $20.6 \times 20.6 \mu\text{m}$ (TiAnd) or 5.6×5.6

460 μm (ServRod) resulting in 24 to 320 times more analyses for the same area. Our new set of algorithms

461 allows the matching of FTIR H_2O maps with EPMA compositional maps pixel by pixel. Therefore

462 correlations based on a mapping approach are typically based on 10'000s to 100'000s of data points,

463 making it possible to have more robust statistics.

464 A prerequisite for the correlation of Ti with H on a molar basis in garnet is to have a well constrained

465 calibration of H_2O absorption in andradite garnet. The published extinction coefficients for garnet

466 vary greatly (from 116 to $14400 \text{ l.mol}^{-1}.\text{cm}^{-2}$, see Reynes et al. 2018 for details). For the Ti-rich

467 andradite core of TiAnd, independent combustion measurements for the H_2O content are available

468 (Müntener and Hermann, 1994). These values are reproduced within error using the extinction

469 coefficient of $14400 \text{ l.mol}^{-1}.\text{cm}^{-2}$ determined for grossular from Maldener et al. (2003), indicating that

470 there is no significant difference in the extinction coefficient between grossular and andradite.

471 ServRod shows a correlation close to 1:1 between $n^*\text{Ti}$ and $n^*\text{H}$ suggesting that there is one Ti for

472 each H in the crystal structure (Fig. 6). This suggests that 2H^+ rather than 4H^+ replace one Si^{4+} in the

473 tetrahedral site. The resulting charge deficiency is then compensated by two Ti^{4+} in an adjacent

474 octahedral site maintaining local charge balance. An alternative substitution would be that 3H^+

475 replace one Si^{4+} , charge balanced by one Ti^{4+} in an octahedral site. This would result in a 1:3

476 correlation between $n^*\text{Ti}$ and $n^*\text{H}$, which is not observed. The sample TiAnd shows three different

1
2 477 slopes in terms of n^*Ti vs n^*H (Fig. 6b). For the low titanium content (TiO_2 ranging from 0.1 to 2
3 478 wt.%) the slope is 1.28. The second domain is characterised by a slope of 1.89 on a range of 1.6 to 3
4 479 wt.% TiO_2 demonstrating a relative excess of Ti in comparison of H in the crystal structure. This is
5
6 480 caused by extra charge of Ti^{4+} in the crystal structure being partially compensated by divalent cations
7
8 481 on the octahedral site (Morimotoite substitution). In the core of the garnet, for n^*H superior to 370
9
10 482 moles/t, only few data points are available taken with ATR detector. The slope obtained is 1.16
11
12 483 suggesting that a majority of Ti is linked with H, but a small portion of Ti could be also compensated
13
14 484 by Morimotoite substitution.
15
16

17
18 485 Relationships between Ti and H in garnet have been previously investigated by Armbruster et al.
19
20 486 (1998) by single crystal X-ray refinement through the category of Ti-rich andradites (1 to 12 wt. %
21
22 487 Ti) – some being similar to our sample TiAnd in terms of titanium content and water. They observed
23
24 488 that the incorporation of the small Ti^{4+} cation in the octahedral site in the garnet structure causes some
25
26 489 distortion favouring the incorporation of bigger cations, such as Fe^{3+} or $(4H)^{4+}$ on the tetrahedral site.
27
28 490 In their study, the extra charge introduced by Ti^{4+} in the garnet structure was thought to be entirely
29
30 491 compensated by Fe^{2+} in the octahedral site (Morimotoite substitution) or Fe^{3+} in tetrahedral site
31
32 492 (Schorlomite substitution). Kühberger et al. (1989) proposed that the OH groups are disposed close to
33
34 493 the sides of the tetrahedron, allowing big cations like Fe^{3+} or Fe^{2+} to sit together with one or two H in
35
36 494 the tetrahedral site in similar Ti-rich garnets. They demonstrated also that the presence of Ti^{4+}
37
38 495 introduces extra charge in the crystal and may be compensated by incomplete silicon vacancy
39
40 496 mechanism with $3H^+$ instead of 4 in the tetrahedral site. Our study is the first to provide quantitative
41
42 497 evidence that only two H occupy the Si-site resulting in a new garnet theoretical hydrous garnet
43
44 498 endmember with the formula $Ca_3Ti_2H_2Si_2O_{12}$ (Table 1).
45
46
47
48
49

50 499

51 52 500 *Recalculation of ferrous and ferric iron in garnet*

53
54 501 The garnet TiAnd has a very high TiO_2 up to 11 wt%, providing a challenge for correct normalisation
55
56 502 due to the large amount of extra charge induced by up 0.7 apfu of Ti. Combining EPMA analysis, X-
57
58 503 ray refinements, Mössbauer spectroscopy and bulk water measurements, Müntener and Hermann
59
60
61
62
63
64
65

1 (1994) were not able to provide charge balanced garnet structural formula. Therefore they proposed
2 that up to half of the Ti present in the Ti-andradite is present as Ti^{3+} to compensate the charge surplus.
3
4 However, XANES spectroscopy on these garnets subsequently showed no evidence for any Ti^{3+}
5
6 (Berry, et al. 2007). Our new data provide an elegant solution to this problem. If H_2O incorporation
7
8 occurs as $(2H)^{2+}$ in the tetrahedral site, then twice more tetrahedral sites are occupied and charge
9
10 balance is easily attained. Thus $(2H)^{2+}$ vs $(4H)^{4+}$ on the tetrahedral site has also consequences for the
11
12 recalculation of Fe^{2+}/Fe^{3+} ratio in garnet.
13
14
15

16 511

19 512 *Implications for H_2O retention in garnet*

21 513 The ServRod sample shows a water content of 200 to 850 ppm H_2O (Fig. 2a) with multiple zoning
22
23 514 preserved during high pressure metamorphism, estimated at 550 ± 60 °C and 2.1 ± 0.3 GPa (Martin et al.
24
25 515 2008). The highest water content is observed in the core of the garnet. Considering the growth of
26
27 garnet during a typical high pressure - low temperature path during subduction, the core of the garnet
28
29 516 has to be growing during prograde metamorphism (e.g. Baxter and Caddick (2013)). Most of the
30
31 517 water incorporated as OH groups in the crystal structure was then incorporated during the first stage
32
33 518 of the garnet growth and kept during the whole metamorphic cycle. Even the later growth zones are
34
35 519 still at 200 ppm H_2O , indicating that during the whole growth of the garnet, OH groups were
36
37 520 incorporated.
38
39 521

42 522 The oscillatory water zonings correlate with the Ti content, and both appear unaffected by diffusion.
43
44 523 Experimental studies on H diffusion in grossular garnet have shown that H potentially diffuses very
45
46 524 fast via a proton-polaron mechanism where the loss of a H is compensated by the oxidation of a Fe^{2+}
47
48 525 to a Fe^{3+} (Kurka et al. 2005; Reynes et al. 2018). Based on these results, a total loss of H in a garnet
49
50 526 grain of 2000 μm diameter would take less than 320 years at the given peak temperature considering
51
52 527 this fast oxidation-related mechanism (Supplementary material S9). As the Alpine subduction rates
53
54 528 are in the order of 1-2 cm/year (Handy, et al. 2010) a temperature above 500 °C was maintained for
55
56 529 several million years. Hydrogen is obviously much more retentive than expected. Higher retentivity
57
58 530 could be explained by very low oxygen fugacity at the eclogitic stage slowing down the diffusion of
59
60
61
62
63
64
65

1 531 hydrogen. Alternatively, because the H is bound by a coupled substitution with Ti, this might lead to a
2 532 higher retentivity. This example demonstrates that in order to apply experimental H diffusivities in
3
4 533 garnet to constrain metamorphic timescales it is important to make sure that the same diffusion
5
6 534 mechanism is considered.
7
8

9 535 A final question is whether the measured H₂O represents the total water incorporated during the
10
11 536 growth of the garnet or whether some H₂O was lost post formation. The measured OH groups in
12
13 537 ServRod garnets are related to only one stable point defect (TiH₂). H in less stable point defects
14
15 538 might have been lost near the peak conditions or upon exhumation and cooling. It can be argued that
16
17 539 the OH region in the spectrum of the sample ServRod is very simple with only 3 peaks, when spectra
18
19 540 up to 8 different peaks have been commonly identified in grossular grown in hydrothermal conditions
20
21 541 (Rossman and Aines 1991).
22
23
24
25

26 542

27 543 **Conclusions**

28
29
30
31 544 The combination of quantitative compositional maps obtained by EPMA and H₂O maps acquired by
32
33 545 FTIR provides constraints on the substitution mechanisms in garnet based on 10'000 to 100'000 data
34
35 546 points. FTIR data also provide critical constraints on the environment of the OH groups in the crystal
36
37 547 structure. A deconvolution algorithm has been designed to provide maps of single peaks that then can
38
39 548 be compared to major and minor element zoning. This new approach has been applied to a grossular-
40
41 549 rich garnet from a high-pressure metaroddingite and a Ti-rich andradite formed during greenschist
42
43 550 facies conditions. In both garnets two H in the tetrahedral site are charge balanced by two Ti on the
44
45 551 octahedral site, resulting in a new hydrous garnet endmember with the formula Ca₃Ti₂H₂Si₂O₁₂.
46
47
48 552 Therefore, twice as many Si-vacancies are produced for the same amount of H₂O compared to the
49
50 553 classical hydro-grossular defect where four hydrogens occupy a tetrahedral site, with unknown effects
51
52 554 on the rheological behaviour of garnet. Our findings impact also on the recalculation of Fe²⁺/Fe³⁺ in
53
54 555 hydrous garnet as the sum of cation is different when only two hydrogens are allocated to a tetrahedral
55
56 556 site. The preservation of fine scale H₂O zoning at the 50 µm scale in the high-pressure garnet provides
57
58 557 evidence for minimal diffusional resetting during the burial and exhumation of subducted oceanic
59
60
61
62
63
64
65

558 crust, indicating that the coupled Ti-H substitution is more retentive than other H defects in garnets
1
2 559 that have been previously investigated in experimental diffusion studies.
3
4

560 Acknowledgments

561

561 We are grateful to G. Bromiley and an anonymous reviewer for their careful reviews, which helped us
562 to improve the presentation of the manuscript, and H. Keppler for editorial handling. This work was
563 financially supported by the Swiss National Science Foundation grant No. 200021_169062 to J.H. and
564 J.R.
565

566

567 **Figure captions**

568 Fig. 1: Element maps acquired by EMPA for sample ServRod. Each map is expressed in atoms per
569 formula units (apfu). Normalisation was done using 24 charges, 8 cations and $(2H)^{2+}$ counting as a
570 cation.
571

572 Fig. 2: Elements maps acquired by EMPA for sample TiAnd. Each map is expressed in atoms per
573 formula units (apfu). Normalisation was done using 24 charges, 8 cations and $(2H)^{2+}$ counting as a
574 cation.
575

576 Fig. 3: Core to rim FTIR spectra in the middle infrared in region $1500-2000\text{ cm}^{-1}$ and $3100-3800\text{ cm}^{-1}$.
577 (a) ServRod sample, (b) TiAnd sample.
578

579 Fig. 4: H_2O content map obtained from FTIR measurements (a, c) and X-ray map of TiO_2 content in
580 wt% (b, d) for sample ServRod and TiAnd, respectively. The dashed black lines represent the
581 positions of the profiles which are displayed in Fig. 3 and for TiAnd the profiles on Fig. 5. Grey
582 dashed rectangular area on subfigure c. corresponds to the area used for map deconvolution presented
583 in Fig. 10. Purple dashed line rectangular shape is delimiting the part used for detailed analysis in Fig.
584 6 a-c-e for ServRod and Fig. 6 b-d-f for TiAnd. Deconvoluted spectra of spots 1 to 4 for ServRod are

585 displayed on Fig. 7 and spots 1 to 4 for TiAnd are displayed on Fig. 8. White zones on maps are
1
2 586 inclusions, artefacts and zones corresponding to another phase than the mineral of interest.

3
4
5 587
6
7
8 588 Fig. 5: Multiple profiles acquired by FTIR and microprobe along the same line. (a) Integrated ATR
9
10 589 (<1 μm penetration) absorbance (blue) and FPA transmission measurement absorbance (red) along the
11
12 590 same profile drawn on Fig. 4c-d. Purple dots are the reference points used to calibrate the penetration
13
14 591 depth of the IR light using the ATR objective. (b) H_2O content profile (in ppm) computed from FTIR-
15
16 592 FPA measurements (in black straight line), water-content profile computed from FTIR-ATR
17
18 593 measurements (in black dashed line) and TiO_2 wt.% profile (in blue).
19
20
21

22 594
23
24
25 595 Fig. 6: Selected parts of the water maps (see Fig. 4 for location) for detailed analysis (a, b). White
26
27 596 zones represent other phases than garnet. (c) and (d): density plot showing $n^*\text{H}$ versus $n^*\text{Ti}$ in mol/t
28
29 597 (see text for meaning of these notations). Each point takes a colour value, which is determined by the
30
31 598 number of points overlapping the marker. Regression lines in red are shown together with coefficient
32
33 599 of determination (R^2). Vertical dashed lines are delimitations of different zones identified on maps (e)
34
35 600 and (f).
36
37
38

39 601
40
41
42 602 Fig. 7: Selected spectra of ServRod with associated deconvolutions. Only the OH stretching region
43
44 603 between 3200 and 3750 cm^{-1} is displayed. The spectra positions are shown in Fig. 2 a. (a) rim
45
46 604 spectrum, (b) and (c) mantle spectra and (d) core spectrum. All spectra are normalised to the thickness
47
48 605 of the sample. Purple round markers are measured signal, blue round markers are the corrected signal
49
50 606 by subtraction of fluid inclusions. The fluid inclusion correspond to a wide Gaussian peak in black,
51
52 607 whereas the three peaks of the deconvolution are narrow Gaussians shown in green. The sum of the
53
54 608 three Gaussians bands is shown in red.
55
56
57

58 609
59
60
61
62
63
64
65

610 Fig. 8: Selected spectra of TiAnd sample with associated deconvolutions. Only the OH stretching
1
2 611 region between 3400 and 3750 cm^{-1} is displayed. The spectra positions are shown in Fig. 2c. (a) Ti
3
4 612 enriched zone in the rim acquired with 15x objective, (b) low Ti zone acquired with 15x objective, (c)
5
6 613 start of the high Ti zone towards the core acquired with 15x objective and (d) core spectra acquired
7
8 614 with ATR objective. The measured data are shown with blue dots, in green the modelled Lorentzian
9
10 615 peaks and in red the sum of the modelled Lorentzian peaks.

11
12
13
14 616
15
16
17 617 Fig. 9: Maps obtained from the deconvolution of the whole FTIR map of ServRod sample. (a) Local
18
19 618 maximum positions of the main peak. (b) Local maximum positions of the third peak. (c) Water map
20
21 619 showing the contributions of the main peak to the total water content determined. (d) Fluid inclusion
22
23 620 density map expressed as area of the fluid inclusion peak for 1 cm thickness.

24
25
26 621 Fig. 10: Maps obtained from the deconvolution of the FTIR map of TiAnd sample with map of
27
28 622 cations occupying the octahedral sites determined from the compositional maps, expressed in apfu.
29
30 623 Only a small representative zone has been plotted, show on Figure 4 c-d. (a) Water content
31
32 624 contributions of the peak at 3563 cm^{-1} (b) of the peak at 3581 cm^{-1} . (c) Ti apfu map. (d) Plot showing
33
34 625 the number of moles/t of Ti versus the number of moles/t of H for peaks 1 and 2. The plot is a density
35
36 626 plot, and only represent a selection of 37,960 analyses (see Fig. 4c-d)).

37
38
39
40 627 Table 1: Garnet endmembers

41
42
43 628 Table 2: Selected microprobe analysis of ServRod sample

44
45
46 629 Table 3: Selected microprobe analysis of TiAnd sample

47
48
49 630

50
51
52 631 **References:**

53 632 Aines R, Rossman G (1984a) The hydrous component in garnets: pyralspites. *American Mineralogist*
54 633 69:1116-1126

55
56 634 Amthauer G, Rossman G (1998) The hydrous component in garnets: pyralspites. *American*
57 635 *Mineralogist* 83:835-840

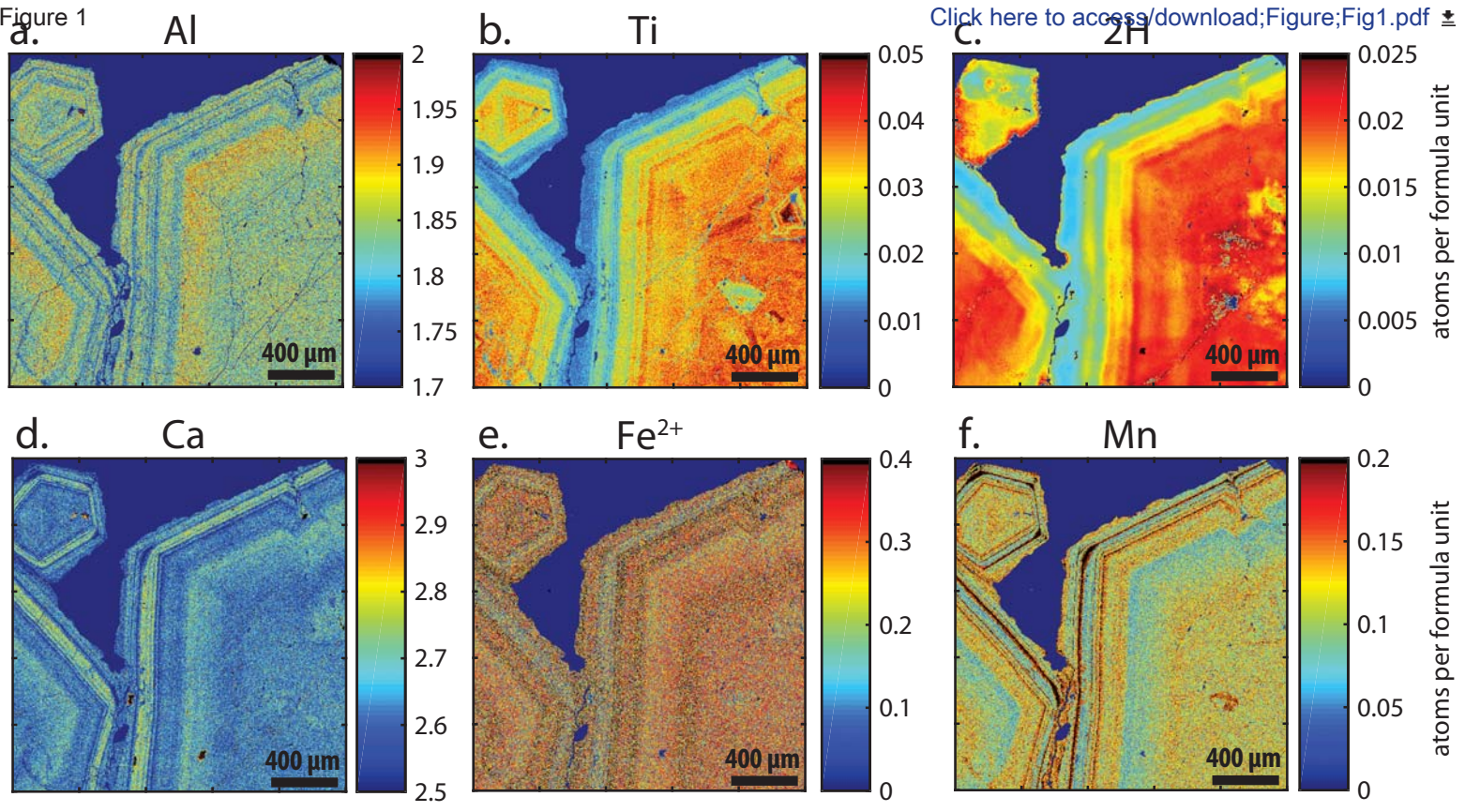
58
59
60
61
62
63
64
65

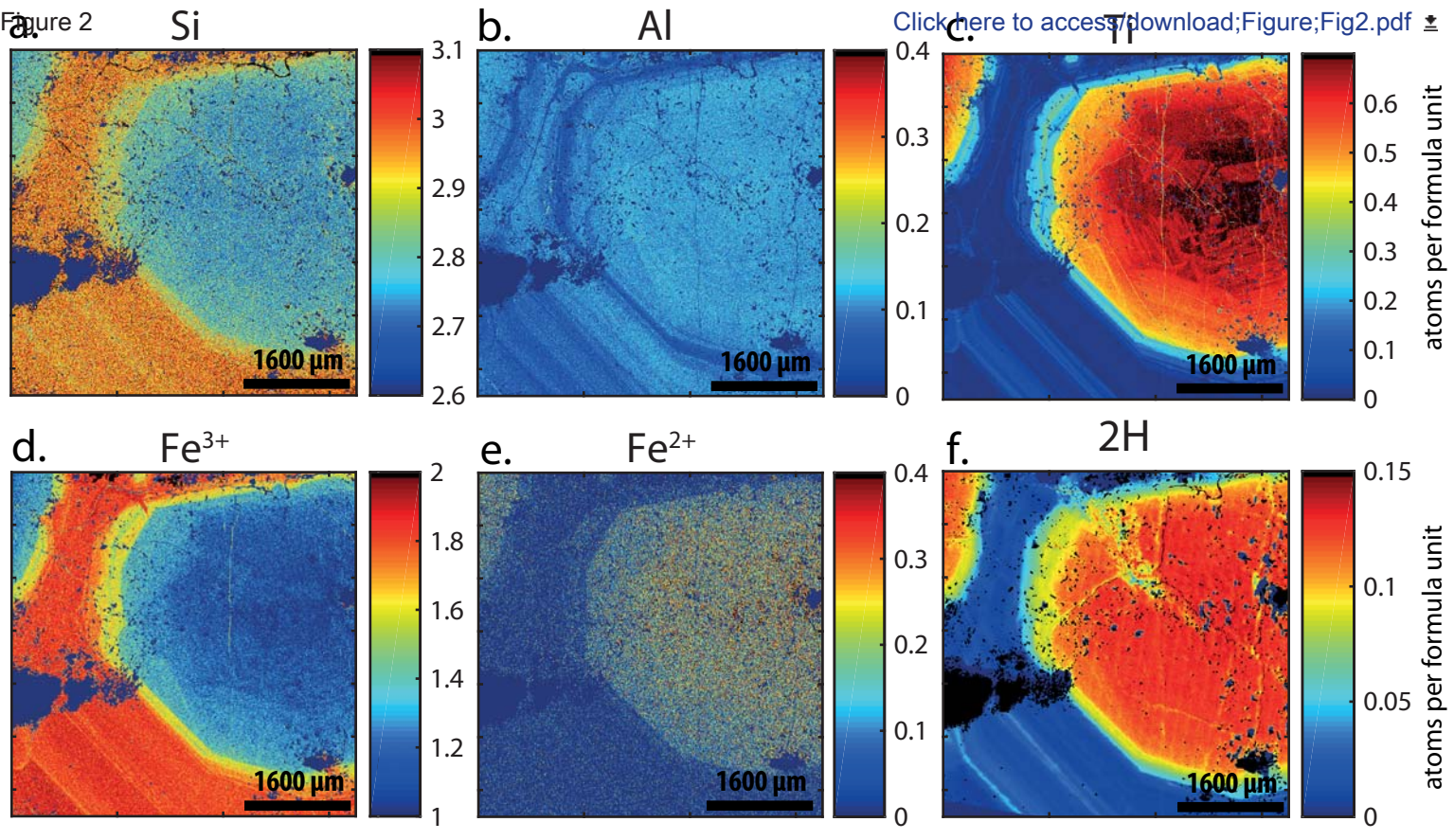
- 636 Andrut M, Wildner M and Beran A (2002) The crystal chemistry of birefringent natural uvarovites.
1 637 Part IV. OH defect incorporation mechanisms in non-cubic garnets derived from polarized IR
2 638 spectroscopy. *European Journal of Mineralogy* 14:1019-1026
3
- 4 639 Armbruster T, Birrer J, Libowitzky E, Beran A (1998) Crystal chemistry of Ti-bearing andradites.
5 640 *European Journal of Mineralogy* 10:907-921
6
- 7 641 Arredondo EH, Rossman GR, Lumpkin GR (2001) Hydrogen in spessartine-alamndine garnets as a
8 642 tracer of granitic pegmatite evolution. *American Mineralogist* 86:485-490
9
- 10 643 Basso R, Cimmino F, Messiga B (1984) Crystal-chemistry of hydrogarnets from 3 different
11 644 microstructural sites of a basaltic metarodingite from the Voltri-massif (Western Liguria, Italy).
12 645 *Neues Jahrbuch Fur Mineralogie-Abhandlungen* 148(3):246-258
13
- 14 646 Baxter E, Caddick M (2013) Garnet growth as a proxy for progressive subduction zone dehydration.
15 647 *Geology* 41(6):643-646
16
- 17 648 Berry A, Walker A, Hermann J, O'Neill H, Foran G, Gale J (2007) Titanium substitution mechanisms
18 649 in forsterite. *Chemical geology* 242:176-186
19
- 20 650 Cohen-Addad C, Ducros P, Bertaut EF (1967) Etude de la Substitution du groupement SiO_4 par $(\text{OH})_4$
21 651 dans les composés $\text{Al}_2\text{Ca}_3(\text{OH})_{12}$ et $\text{Al}_2\text{Ca}_3(\text{SiO}_4)_{2.16}(\text{OH})_{3.36}$ de type grenat. *Acta Crystallographica*
22 652 23:220-230
23
- 24 653 Foreman D (1968) Neutron and X- Ray Diffraction Study of $\text{Ca}_3\text{Al}_2(\text{O}_4\text{D}_4)_3$, a Garnetoid. *J Chem*
25 654 *Phys* 48:3037-3041
26
- 27 655 Geiger CA, Langer K, Bell DR, Rossman GR, Winkler B (1991) The hydroxide component in
28 656 synthetic pyrope. *American Mineralogist* 76:49-59
29
- 30 657 Geiger CA, Rossman GR (2018) IR spectroscopy and OH⁻ in silicate garnet: The long quest to
31 658 document the hydrogarnet substitution. *American Mineralogist* 103:384-393
32
- 33 659 Handy MR, Schmid SM, Bousquet R, Kissling E, Bernoulli D (2010) Reconciling plate-tectonic
34 660 reconstructions of Alpine Tethys with the geological-geophysical record of spreading and subduction
35 661 in the Alps. *Earth-Science Reviews* 102:121-158
36
- 37 662 Johnson EA (2003) Hydrogen in nominally anhydrous crustal minerals. Dissertation, California
38 663 institute of technology
39
- 40 664 Jollands M, Hermann J, Müntener O (2019) Coupled inter-site reaction and diffusion: Rapid
41 665 dehydrogenation of silicon vacancies in natural olivine. *Geochimica et Cosmochimica Acta* 262:220-
42 666 242
43
- 44 667 Khomenko VM, Langer K, Beran A, Koch-Müller M, Fehr T (1994) Titanium Substitution and OH-
45 668 Bearing Defects in Hydrothermally Grown Pyrope Crystals. *Physics and Chemistry of Minerals*
46 669 20:483-488
47
- 48 670 Kühberger A, Fehr T, Huckenholz HG, Amthauer G (1989) Crystal Chemistry of a Natural
49 671 Schorlomite and Ti-Andradites Synthetized at Different Oxygen Fugacities. *Physics and Chemistry of*
50 672 *Minerals* 16:734-740
51
- 52 673 Kurka A, Blanchard M, Ingrin J (2005) Kinetics of hydrogen extraction and deuteration in grossular.
53 674 *Mineralogical Magazine* 69(3):359-371
54
- 55 675 Lager GA, Armbruster T, Faber J (1987) Neutron and X-ray diffraction study of hydrogarnet
56 676 $\text{Ca}_3\text{Al}_2(\text{O}_4\text{H}_4)_3$. *American Mineralogist* 72:756-765
57
- 58 677 Lanari P, Vidal, O., De Andrade V, Dubacq B, Lewin EG, Schwartz S (2014) XMapTools: A
59 678 MATLAB-based program for electron microprobe X-ray image processing and geothermobarometry.
60 679 *Computers & Geosciences* 62:227-240
61
62
63
64
65

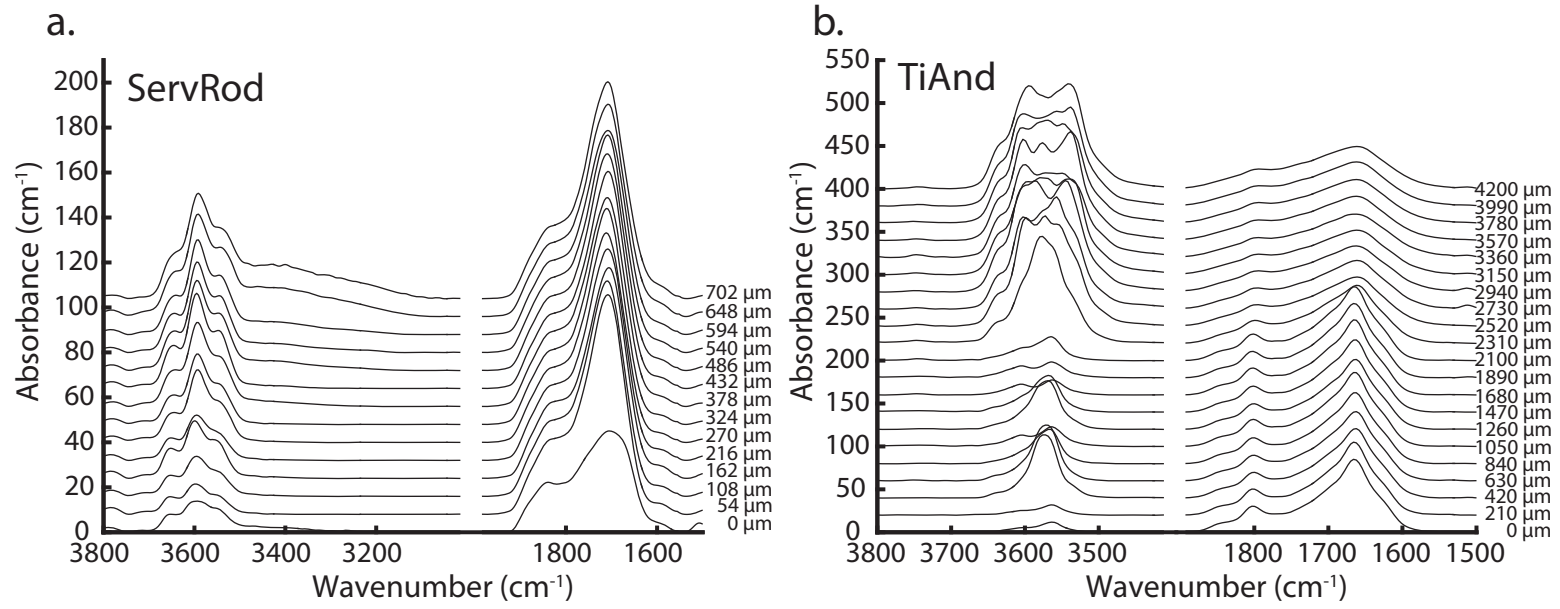
680 Lanari P, Vho, A. Bovay T, Airaghi L, Centrella S (2019) Quantitative compositional mapping of
1 681 mineral phases by electron probe micro-analyser. In: Ferrero S, Goncalves P, Grosch E (ed)
2 682 Metamorphic Geology: Microscale to Mountain Belts, vol 478. Geological Society of London,
3 683 Special Publications.
4
5 684 Lu R, Keppler H (1997) Water solubility in pyrope to 100 kbar. Contributions to Mineralogy and
6 685 Petrology 129:35-42
7 686
8 687 Maldener J, Hösch A, Langer K, Rauch F (2003) Hydrogen in some natural garnets studied by nuclear
9 688 reaction analysis and vibrational spectroscopy. Physics and Chemistry of Minerals 30:337-344
10 689
11 690 Martin S, Rebay G, Kienast J-R, Mével C (2008) An eclogitised oceanic palaeo-hydrothermal field
12 691 from the St. Marcel Valley (Italian Western Alps). Ofioliti 33(1):49-63
13 692
14 693 Müntener O, Hermann J (1992) Titanian andradite in a metapyroxenite layer from the Malenco
15 694 ultramafics (italy): implications for Ti-mobility and low oxygen fugacity. Contrib Mineral Petrol
16 695 116:156-168
17 696
18 697 O'Haver T (2015) A Pragmatic* Introduction to Signal Processing with applications in scientific
19 698 measurement; An illustrated essay with free software and spreadsheet templates to download.
20 699 <https://terpconnect.umd.edu/~toh/spectrum/>.
21 700
22 701 Reynes J, Jollands MC, Hermann J, Ireland T (2018) Experimental constraints on hydrogen diffusion
23 702 in garnet. Contributions to mineralogy and Petrology 173(69):68-70
24 703
25 704 Rossman GR, Aines RD (1991) The hydrous components in garnets: Grossular-hydrogrossular.
26 705 American Mineralogist 76:1153-1164
27 706
28 707 Tartarotti P, Martin S, Monopoli B, Benciolini L, Schiavo A, Campana R, Vigni I (2017) Geology of
29 708 the Saint-Marcel valley metaophiolites (Northwestern Alps, Italy), Journal of Maps, 13:2, 707-717
30
31
32
33
34
35
36
37
38
39
40
41
42
43
44
45
46
47
48
49
50
51
52
53
54
55
56
57
58
59
60
61
62
63
64
65

Figure 1

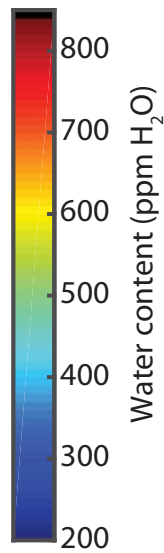
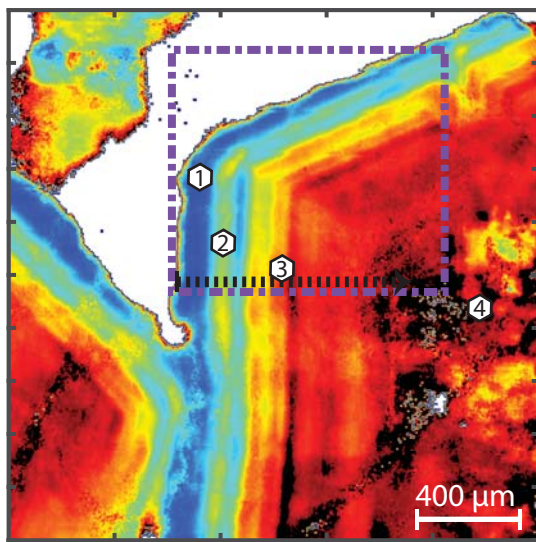
[Click here to access/download;Figure;Fig1.pdf](#)



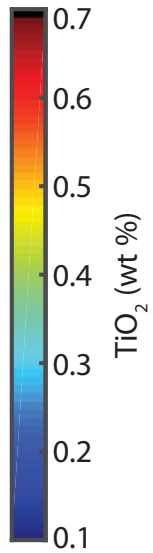
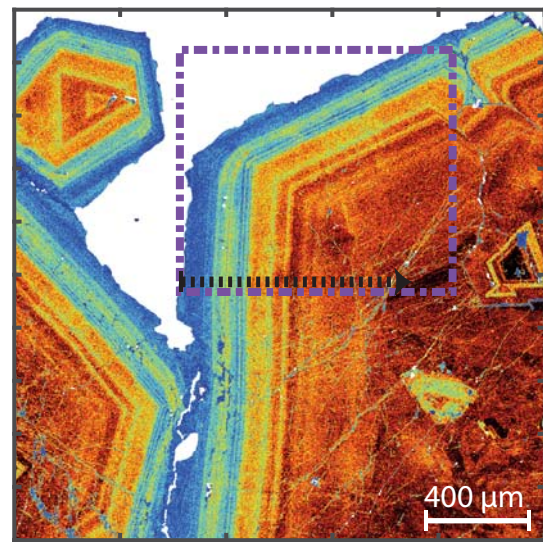




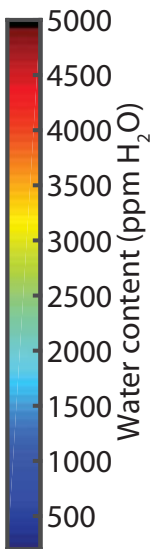
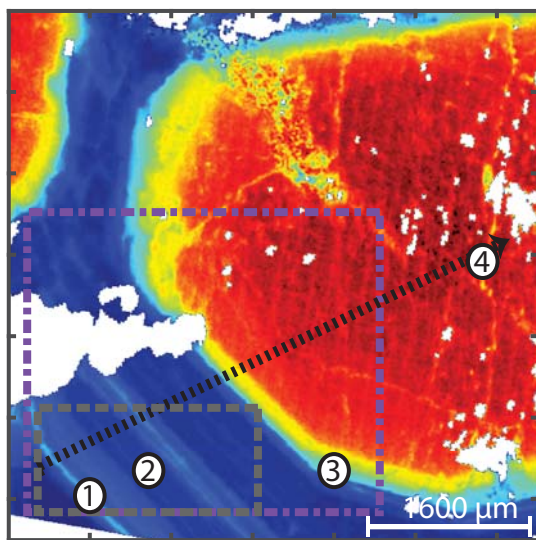
a. ServRod



b.



c. TiAnd



d.

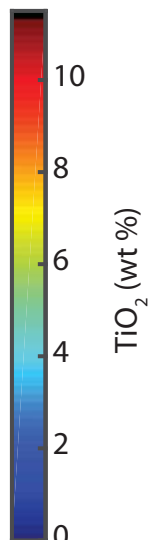
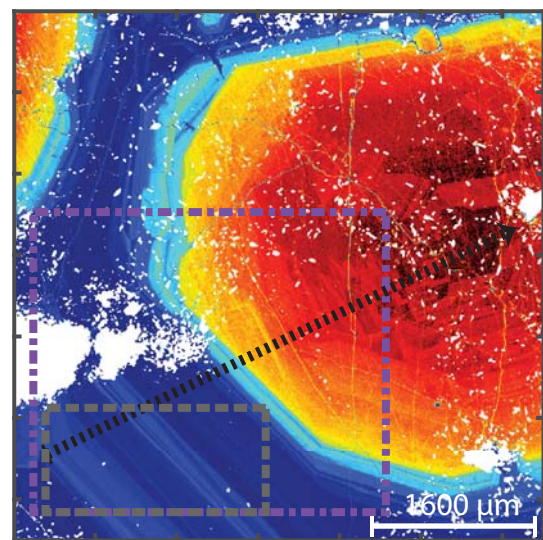


Figure 5

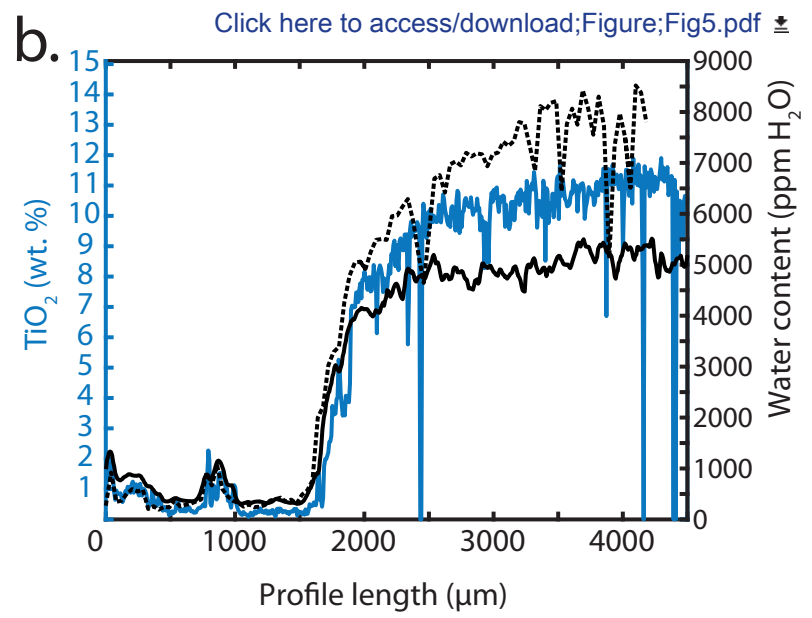
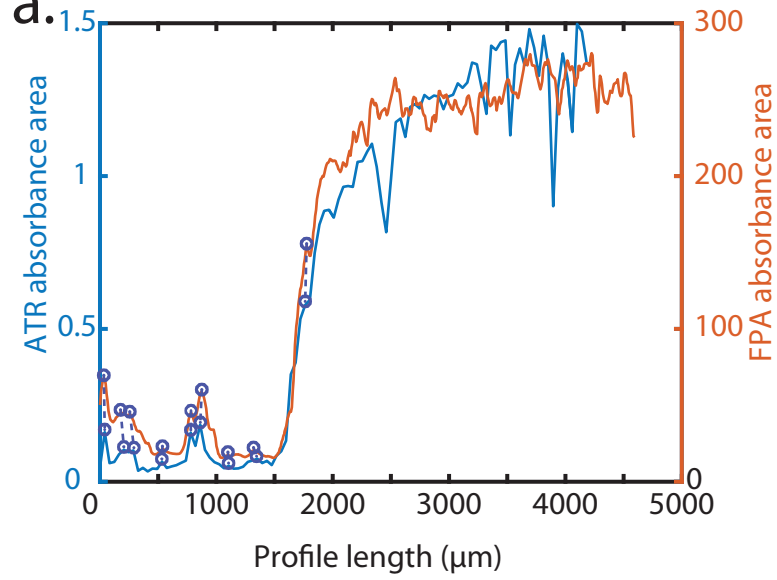
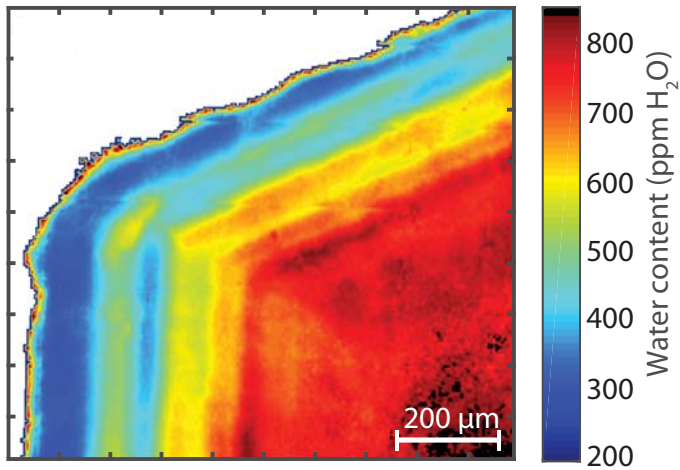


Figure 6

[Click here to access/download;Figure;Fig6.pdf](#)

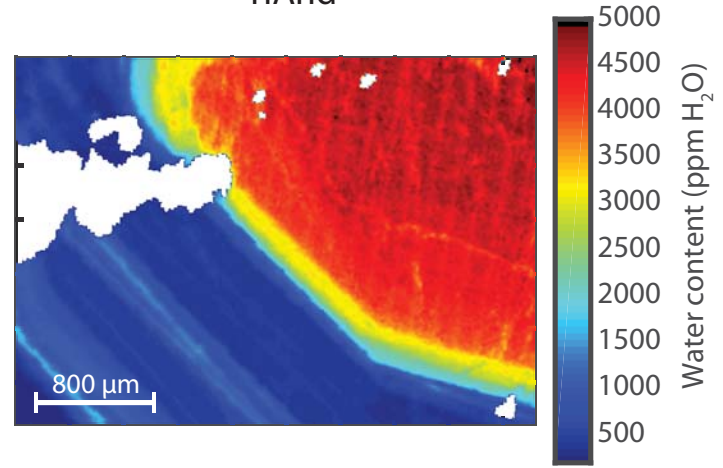
a.

ServRod

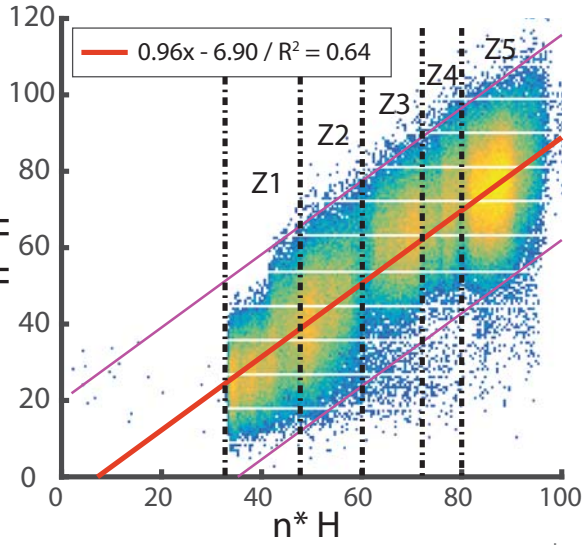


b.

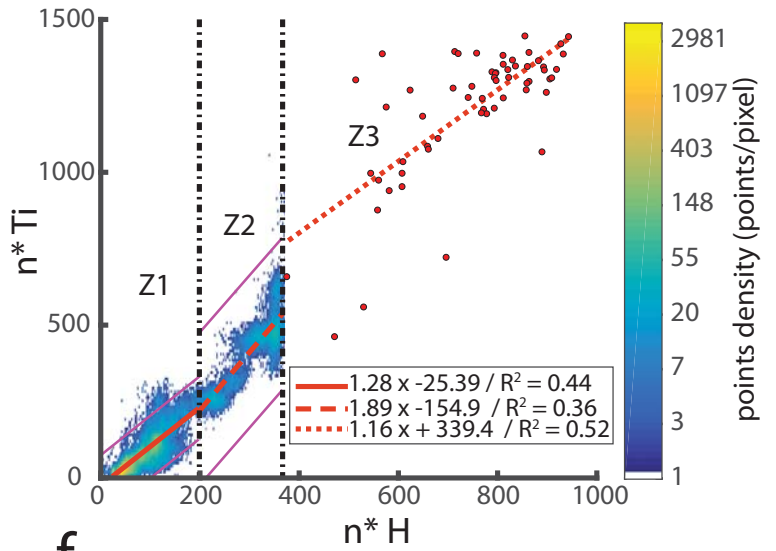
TiAnd



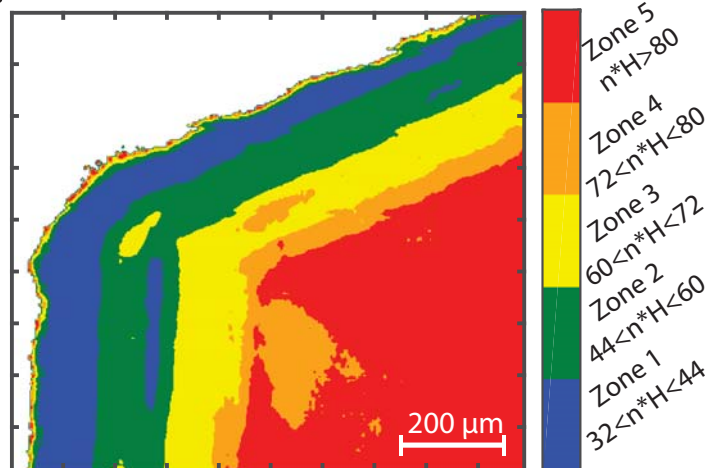
c.



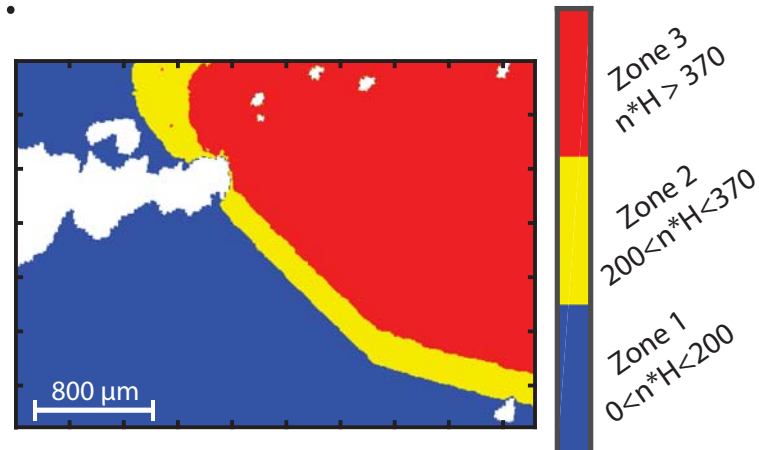
d.



e.



f.



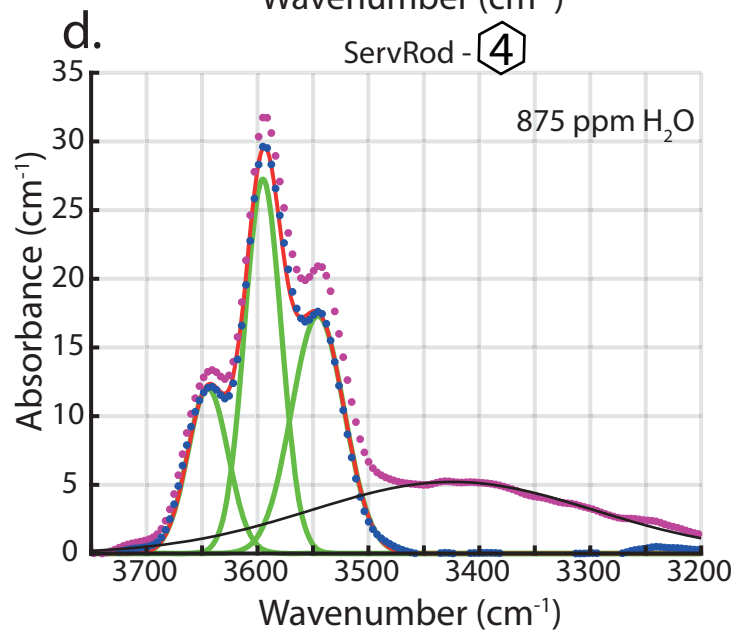
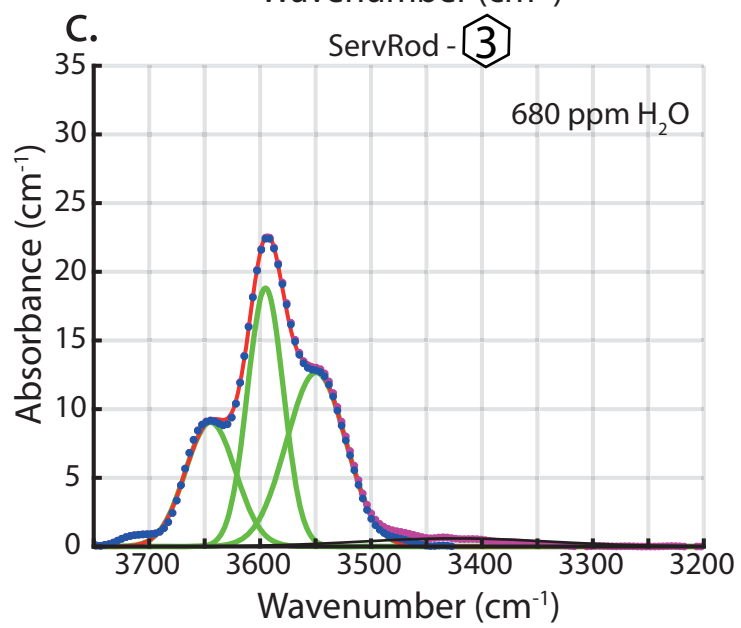
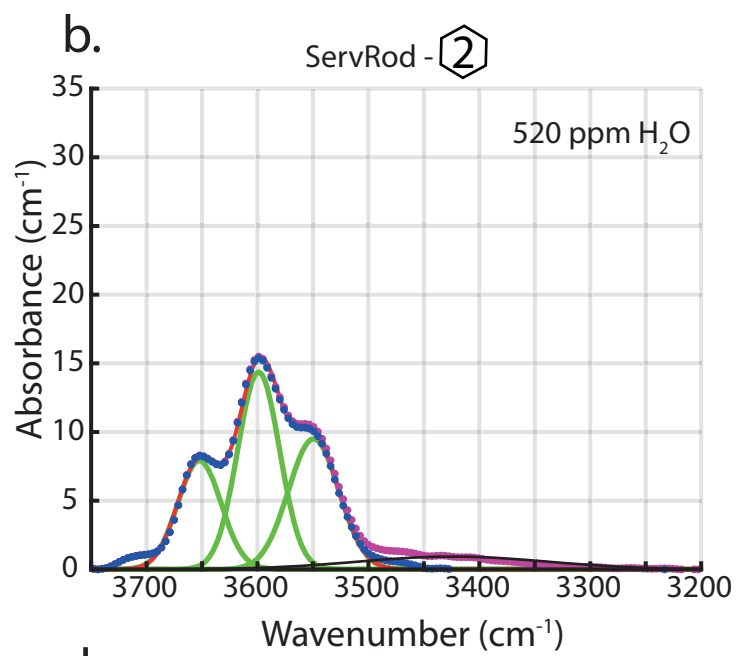
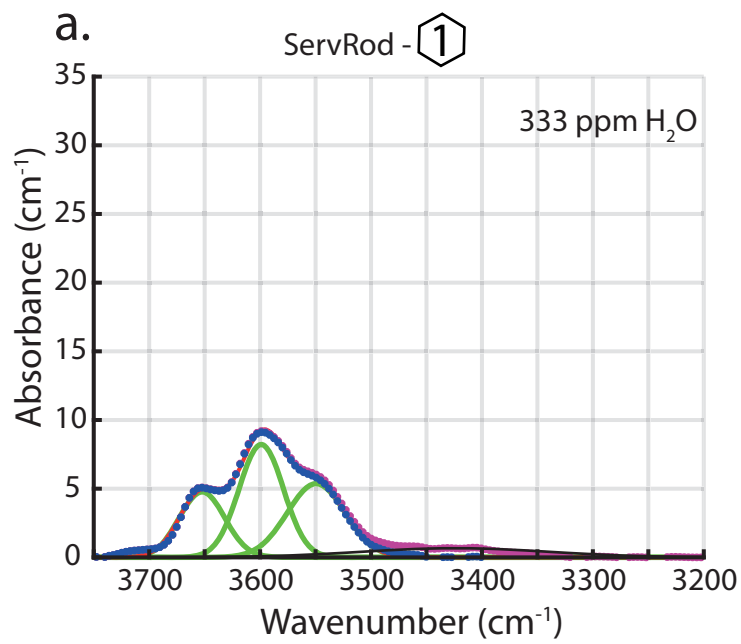
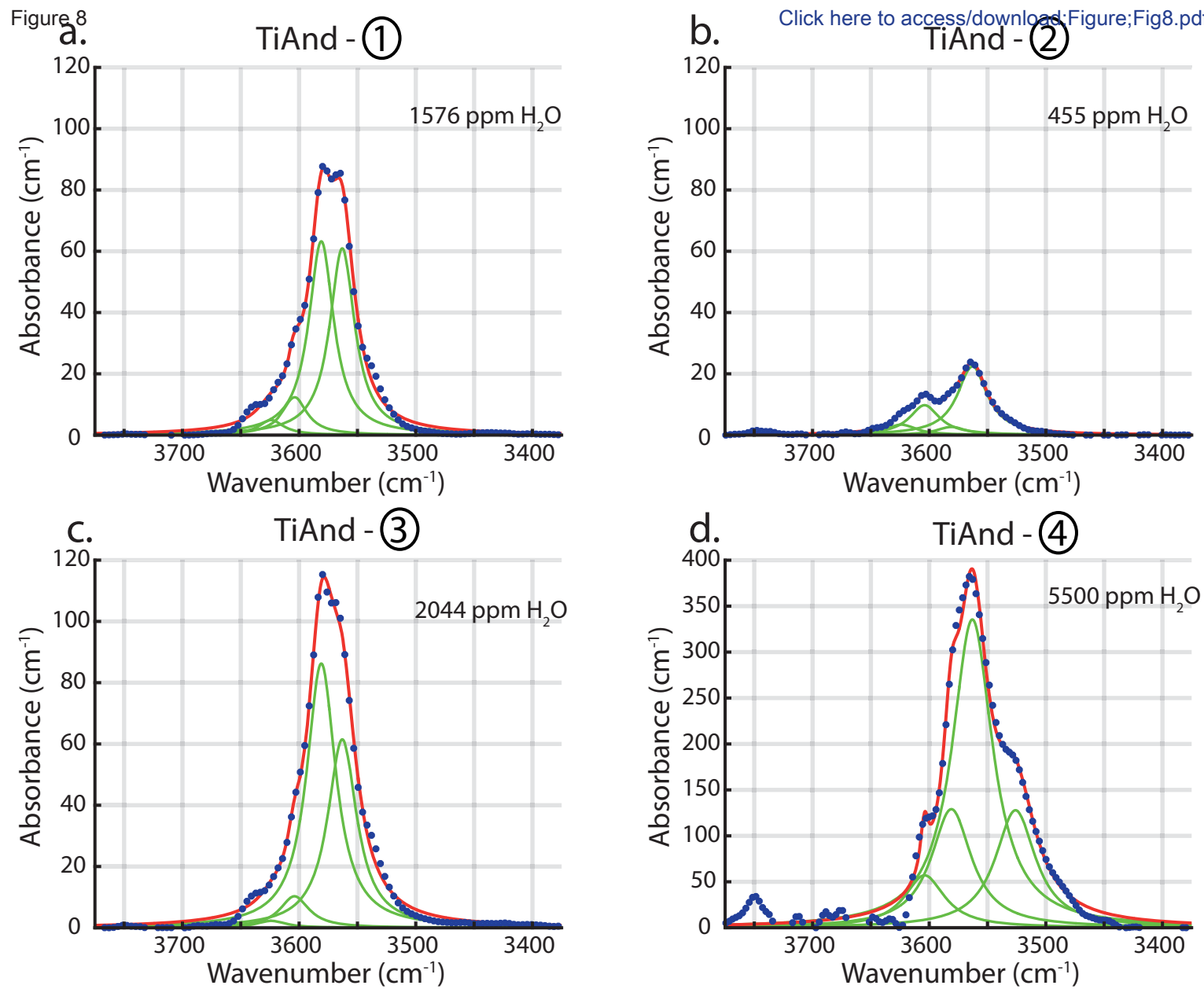
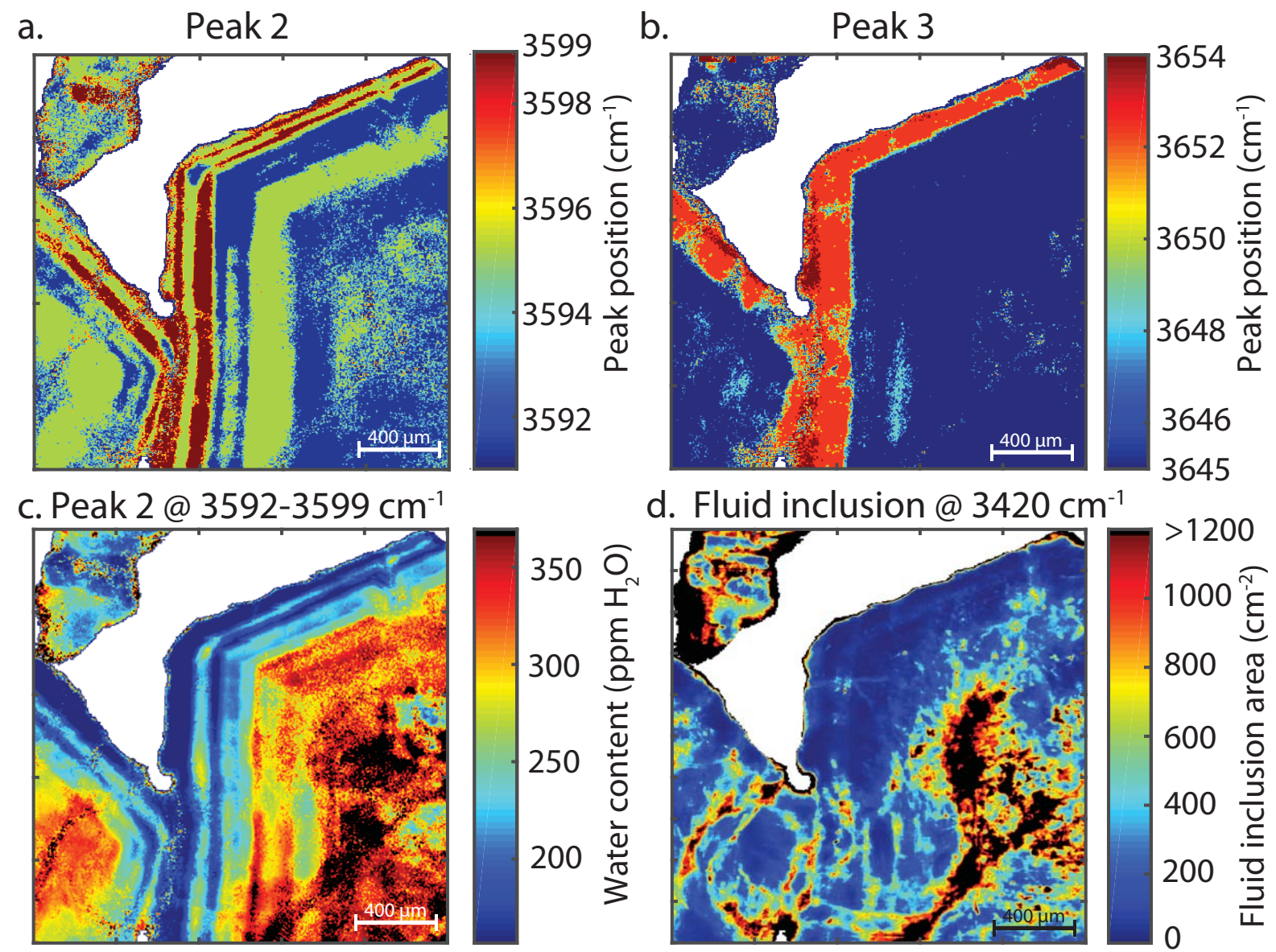
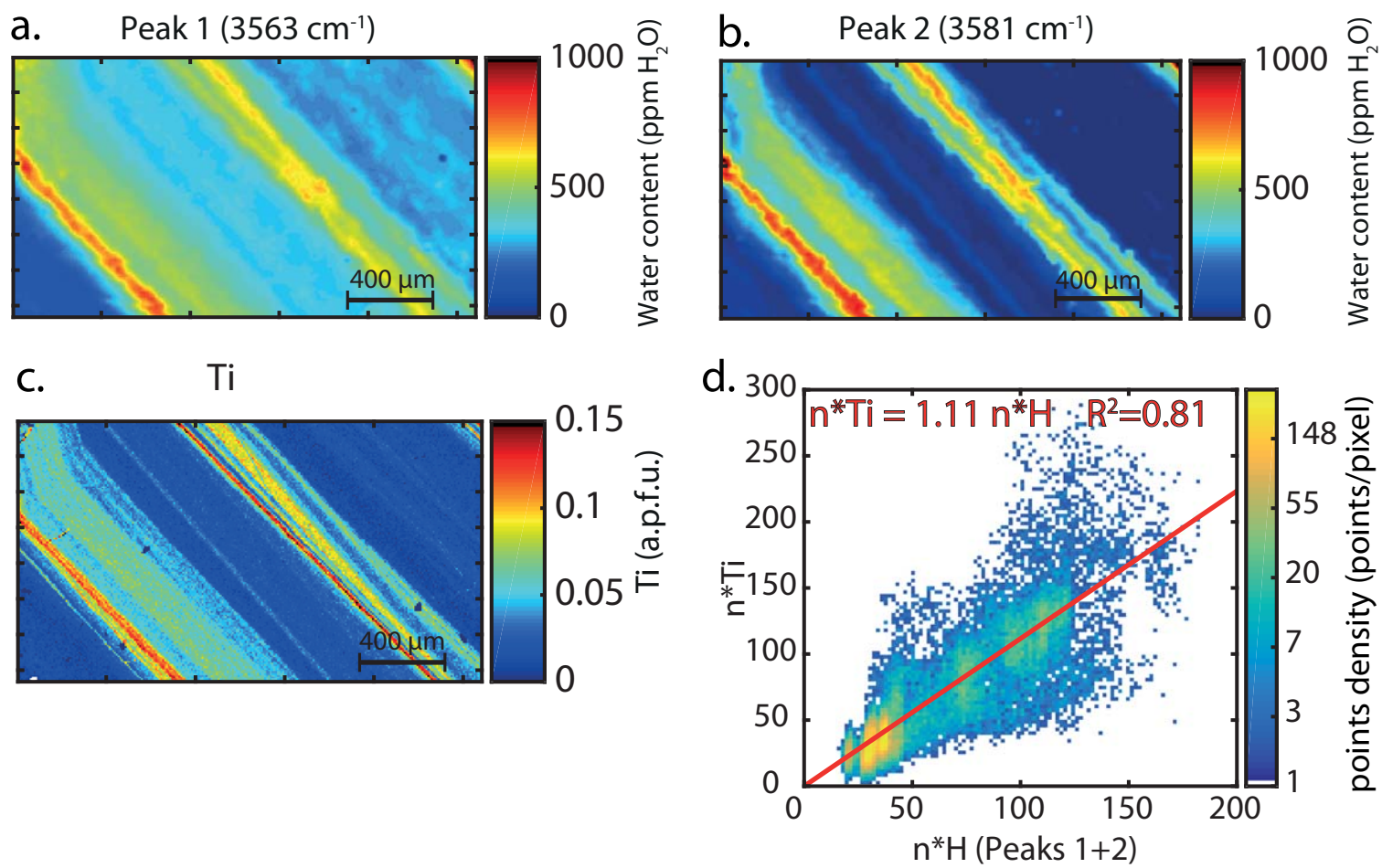


Figure 8

[Click here to access/download:Figure;Fig8.pdf](#)





Dry endmembers	
$\text{Ca}_3\text{Al}^{3+}_2[\text{Si}_3]\text{O}_{12}$	Grossular
$\text{Ca}_3\text{Fe}^{3+}_2[\text{Si}_3]\text{O}_{12}$	Andradite
$\text{Ca}_3\text{Fe}^{2+}\text{Ti}^{4+}[\text{Si}_3]\text{O}_{12}$	Morimotoite
$\text{Ca}_3\text{Fe}^{3+}\text{Ti}^{4+}[\text{Fe}^{3+}\text{Si}_2]\text{O}_{12}$	Schorlomite
$\text{Ca}_3\text{Fe}^{3+}\text{Ti}^{4+}[\text{Al}^{3+}\text{Si}_2]\text{O}_{12}$	<i>Al-TiAndradite</i>
Hydrous endmembers	
$\text{Ca}_3\text{Al}^{3+}_2[\text{H}_4\text{Si}_2]\text{O}_{12}$	Hydrogrossular
$\text{Ca}_3\text{Fe}^{3+}_2[\text{H}_4\text{Si}_2]\text{O}_{12}$	Hydroandradite
$\text{Ca}_3\text{Ti}^{4+}_2[\text{H}_2\text{Si}_2]\text{O}_{12}$	<i>Ti-hydrogarnet</i>

ServRod	Point1	Point2	Point3	Point4
SiO₂	39.65	39.29	38.65	38.69
Al₂O₃	20.38	20.30	20.20	20.46
Cr₂O₃	0.00	0.00	0.00	0.00
TiO₂	0.15	0.33	0.62	0.77
FeOt	6.49	4.69	4.77	5.91
FeOc	3.85	2.03	2.73	3.85
Fe₂O_{3c}	2.94	2.96	2.27	2.30
MnO	2.89	0.87	1.59	0.72
MgO	0.00	0.00	0.18	0.37
CaO	31.38	34.61	32.69	32.54
H₂O	0.03	0.05	0.07	0.09
Total	101.23	100.47	99.02	99.83
Si	3.010	2.983	2.979	2.958
2H	0.008	0.013	0.018	0.022
Al^{Tetra}	0.000	0.004	0.003	0.020
Σ Tetra	3.018	3.000	3.000	3.000
Al	1.823	1.812	1.832	1.824
Ti	0.009	0.019	0.036	0.044
Fe³⁺	0.168	0.169	0.132	0.132
Σ Oct	2.000	2.000	2.000	2.000
Fe²⁺	0.244	0.129	0.176	0.246
Mn	0.186	0.056	0.104	0.047
Mg	0.000	0.000	0.021	0.042
Ca	2.552	2.815	2.700	2.665
Σ Dod	2.982	3.000	3.000	3.000
Σ Charges	24.03	23.99	24.00	23.98
Σ Cations	8.000	8.000	8.000	8.000

Ti And	Point1	Point2	Point3	Point4	Point5
SiO₂	35.22	35.70	34.25	34.07	32.85
Al₂O₃	0.85	0.87	0.98	1.05	1.13
Cr₂O₃	0.47	0.42	0.16	0.29	0.22
TiO₂	0.82	2.05	4.85	7.67	11.24
FeOt	26.31	25.02	22.59	20.86	17.80
FeOc	0.11	0.52	0.29	1.36	2.05
Fe₂O_{3c}	29.12	27.23	24.78	21.67	17.50
MnO	0.00	0.00	0.47	0.19	0.32
MgO	0.02	0.64	0.27	0.28	0.51
CaO	33.05	32.95	33.25	33.78	33.28
H₂O	0.06	0.13	0.34	0.55	0.84
Total	99.24	100.51	99.65	100.90	99.94
Si	2.983	2.979	2.869	2.814	2.707
2H	0.017	0.037	0.094	0.151	0.231
Al^{tetra}	0.000	0.000	0.037	0.035	0.062
Σ Tetra	3.001	3.015	3.000	3.000	2.999
Al^{Oct}	0.080	0.086	0.060	0.065	0.048
Ti	0.052	0.129	0.305	0.472	0.702
Fe³⁺	1.842	1.699	1.555	1.329	1.074
Fe²⁺	0.016	0.047	0.027	0.108	0.149
MgMn^{Oct}	0.003	0.040	0.052	0.025	0.027
Σ Oct	1.993	2.000	1.999	1.999	2.000
Mg^{Dod}	0.000	0.040	0.000	0.005	0.033
Mn	0.000	0.000	0.016	0.010	0.020
Ca	2.999	2.945	2.984	2.985	2.947
Σ Dod	2.999	2.985	3.000	3.000	3.000
Σ Charges	23.980	24.000	24.000	24.000	24.000
Σ Cations	7.993	8.000	8.000	7.999	8.000

Supplementary online material for the article

"A mapping approach for the investigation of Ti-OH relationships in metamorphic garnet" by J. Reynes, P. Lanari and J. Hermann, published in Contributions to Mineralogy and Petrology

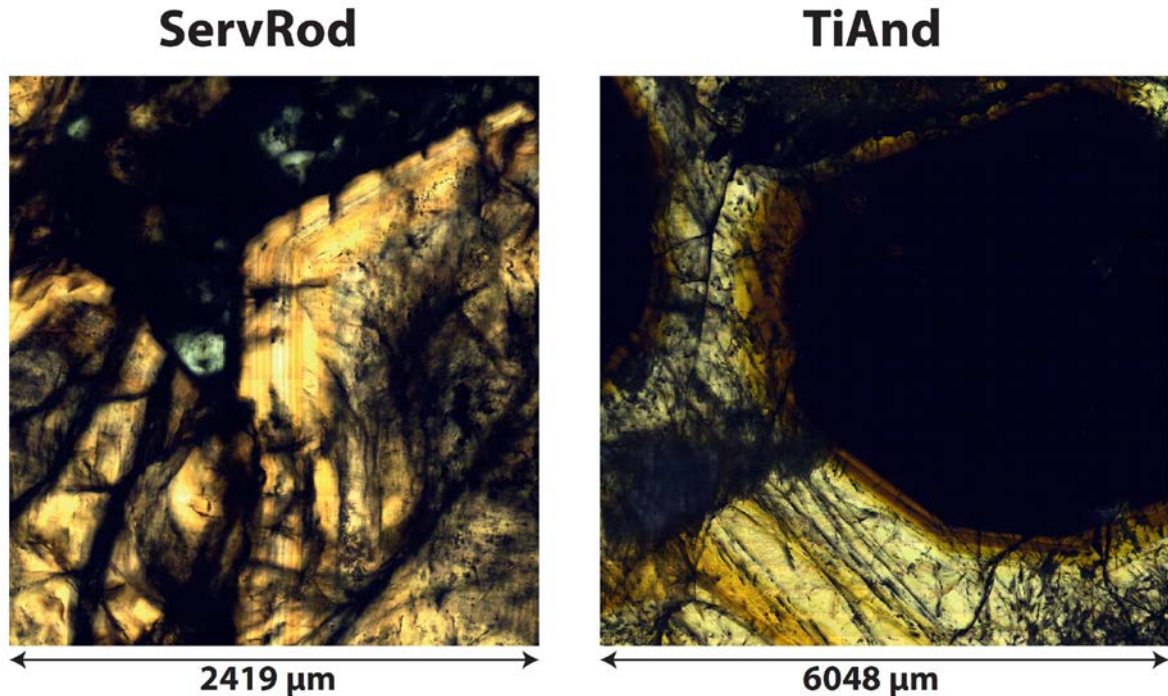


Figure S1: Left side: Picture of analysed zone of ServRod garnet taken with optical transmission microscope.

Chemical zonings are visible, with alternative yellow and orange sharp zones.

Right side: Picture of analysed zone of TiAnd garnet taken with optical transmission microscope.

Core zone is nearly opaque in visible light. Zoning corresponding to higher Ti zones are visible in the rim.

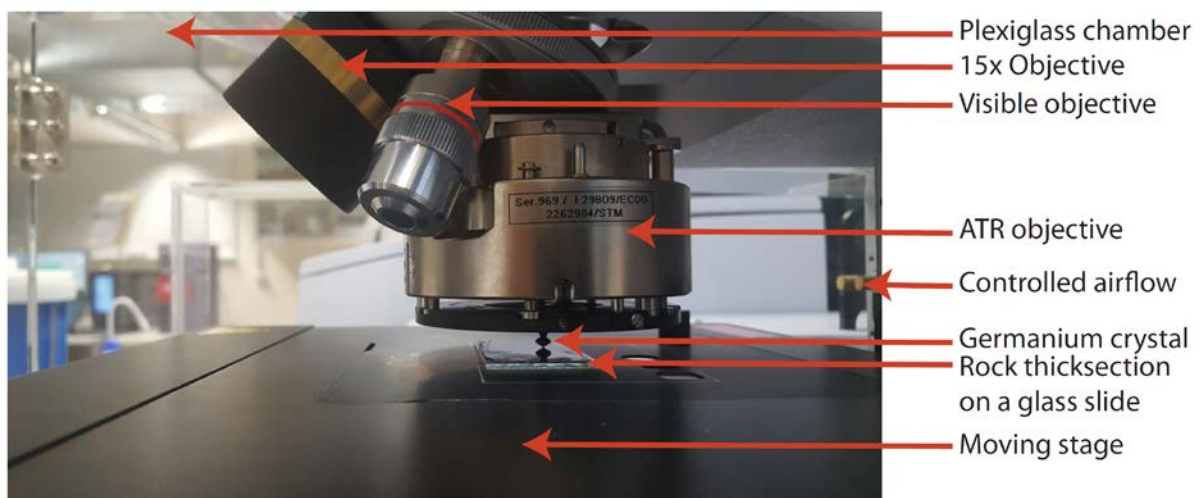


Figure S2: Schema showing the organisation of the different objectives equipped on the FTIR spectrometer. The ATR objective, enabling near surface measurement, is set in position for analysis.

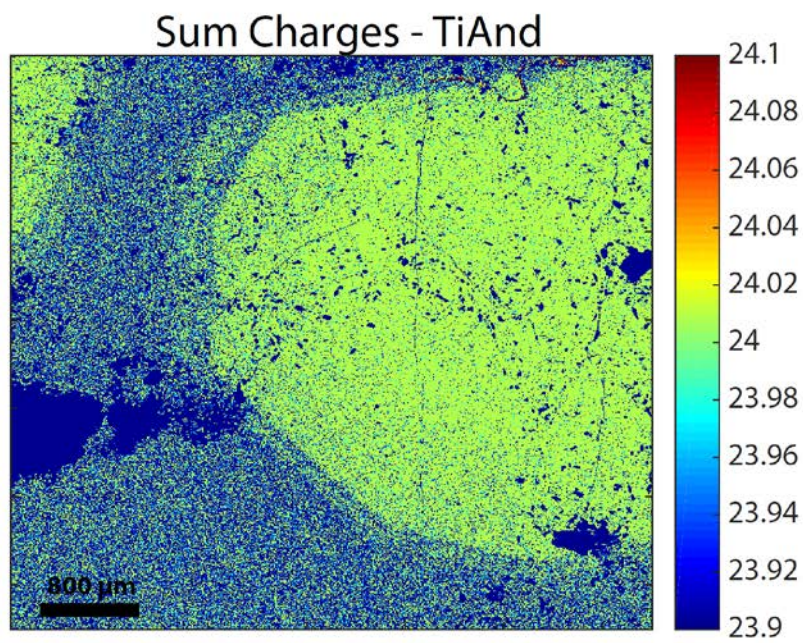
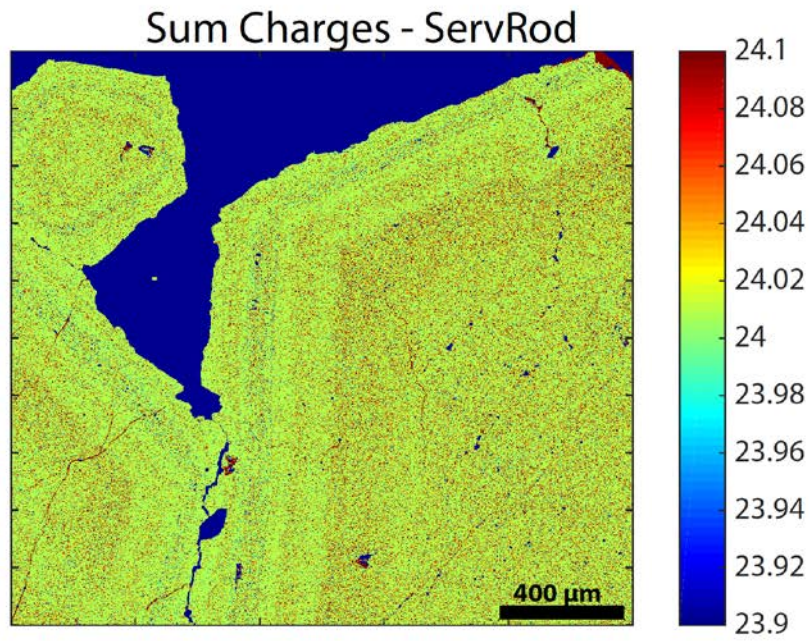


Figure S3: Maps of Sum of charges for both samples issued from structural formula computation program GarnetH2O.

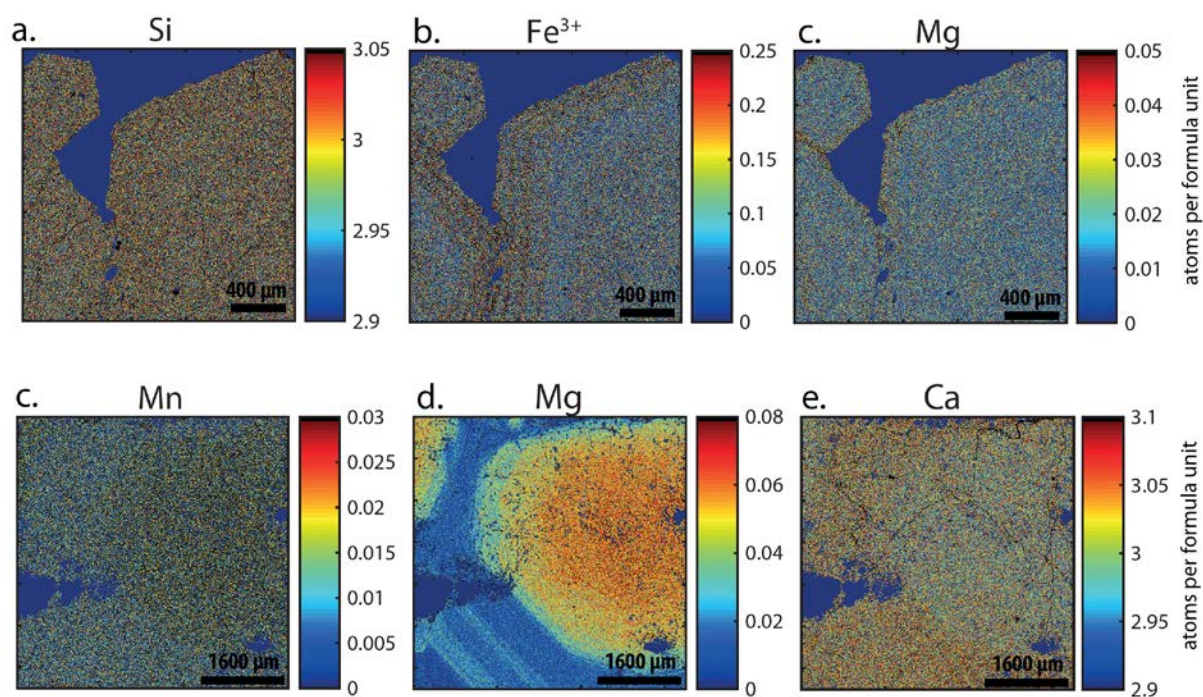


Figure S4: Element maps acquired by EMPA for sample ServRod (a,b,c) and TiAnd (c,d,e). Each map is expressed in atoms per formula units (apfu). Normalisation was done using 24 charges, 8 cations and $(2H)^{2+}$ counting as a cation.

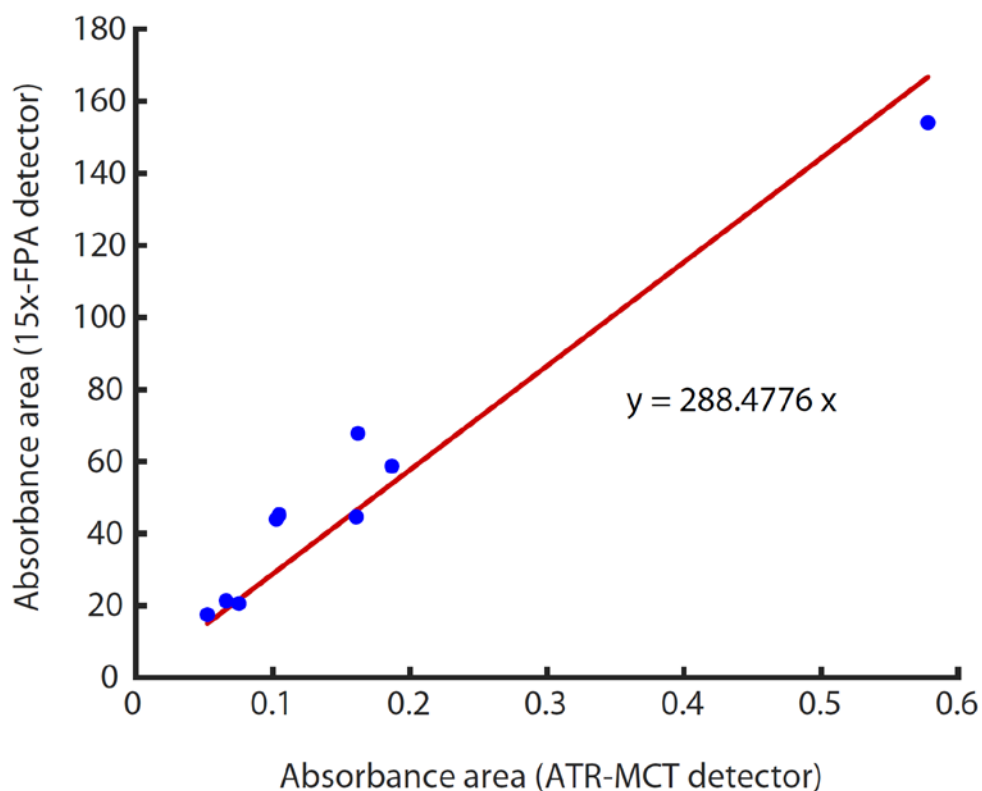


Figure S5: Absorbance area measured by 15x-FPA detector versus the absorbance area measured by ATR-MCT detector. Knowing the thickness of the sample (162 μm), it is possible to deduce the penetration depth of the ATR beam (0.56 μm).

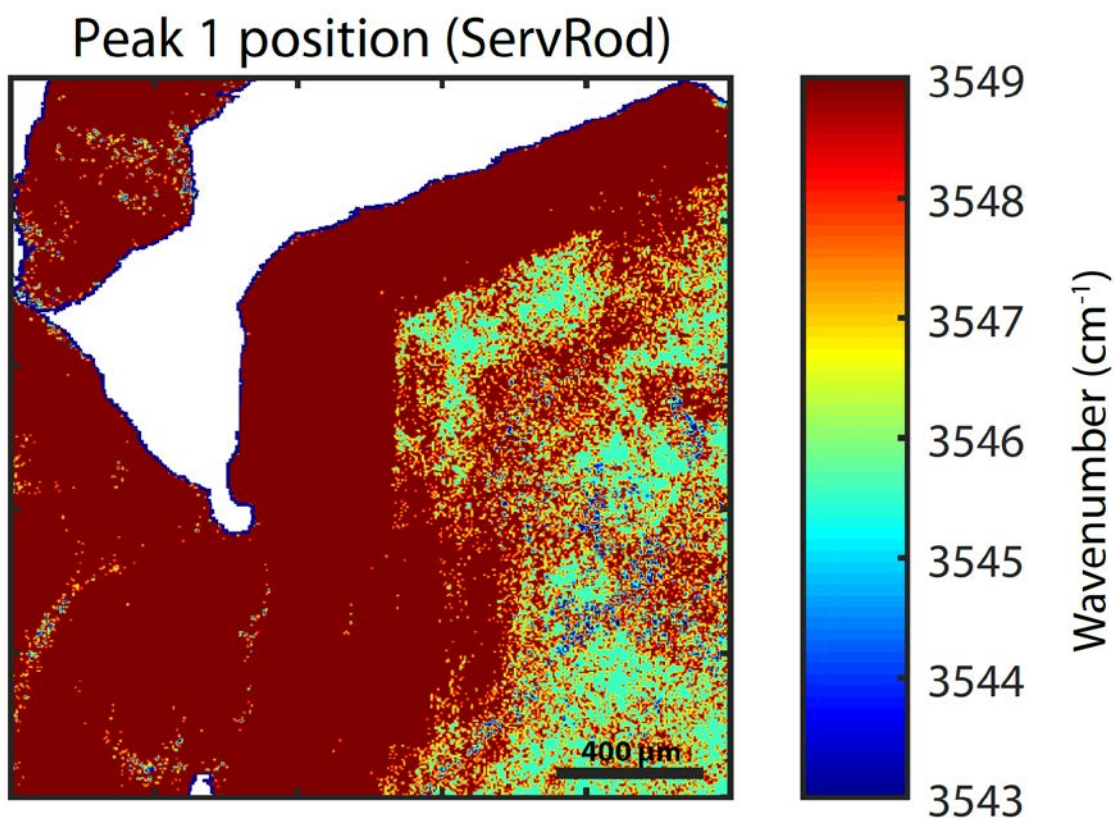


Figure S6: Peak 1 positions (Local maxima) in the domain 3543-3549 cm^{-1} of the IR spectra for ServRod sample.

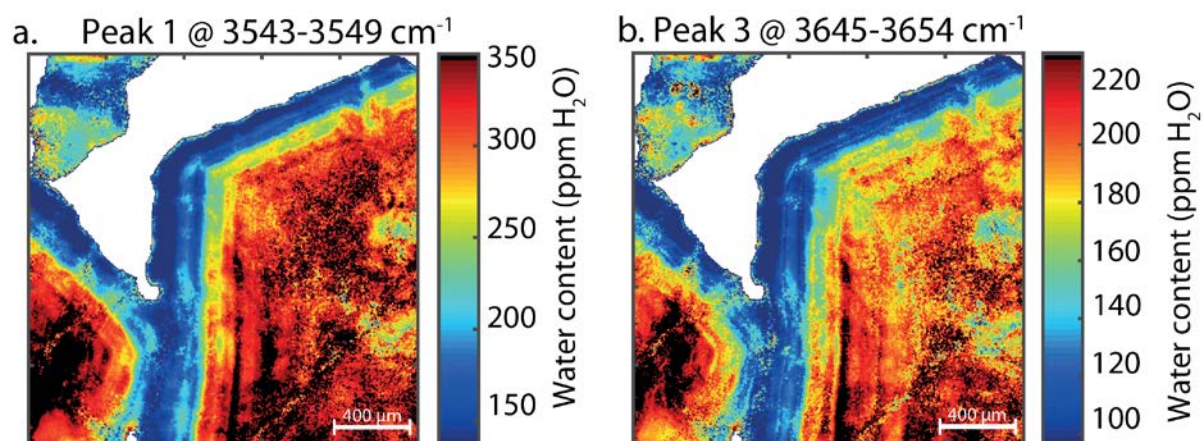


Figure S7: Deconvolution map of peaks 1 and 3 for the sample ServRod. The maps are expressed in ppm.wt H_2O . This figure is a complementary of figure 9.

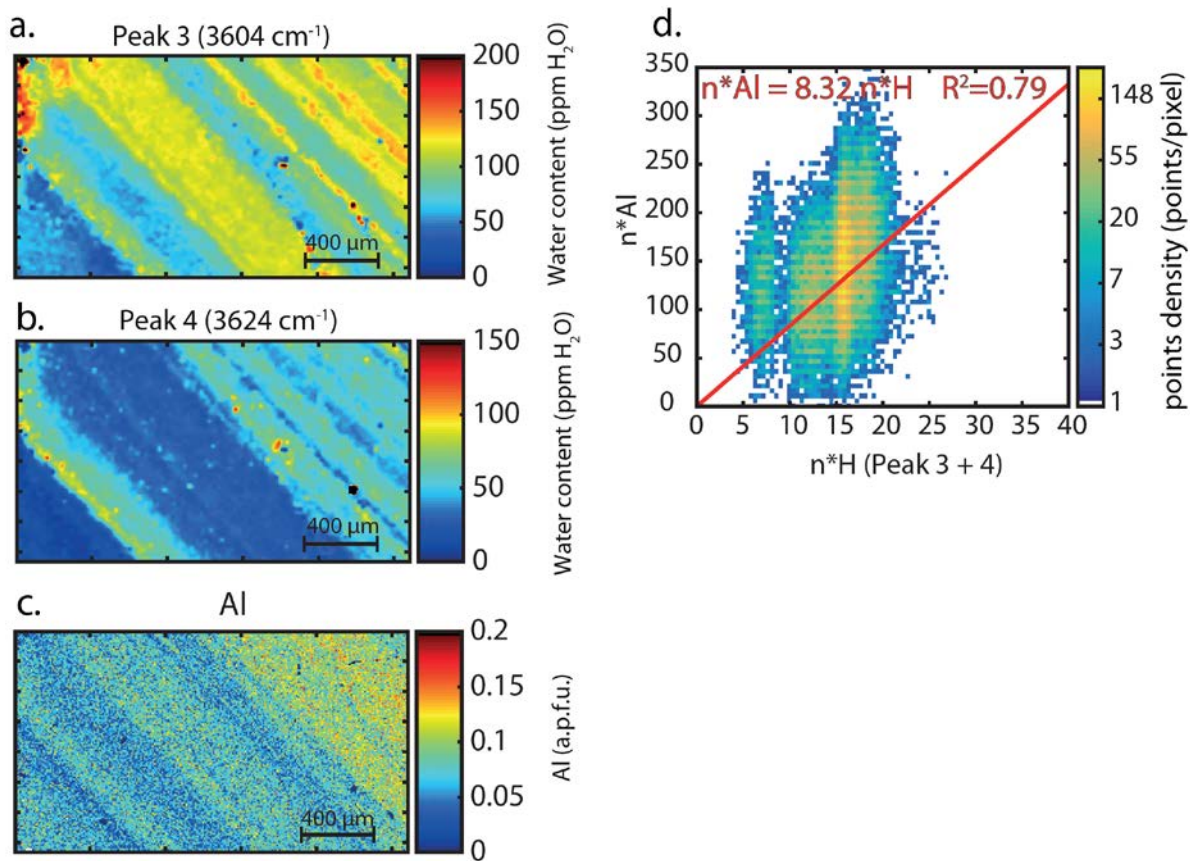


Figure S8: Maps obtained from the deconvolution of the FTIR map of TiAnd sample with map of Al^{3+} occupying the octahedral site determined from the compositional maps, expressed in apfu. Only a small representative zone has been plotted, shown on Figure 4 c-d. Water content contributions of the peak at 3604 cm^{-1} (a) of the peak at 3624 cm^{-1} (b) are displayed. On (d) is plotted the number of moles/t of Al versus the number of moles/t of H for peaks 3 and 4. Both plots are shown as density plots, and only represent a selection of 37,960 analyses. This figure is a complementary figure of figure 10.

Figure S9: see attached a video of 2D H diffusion model on a zoned garnet of $2000\text{ }\mu\text{m}$ in diameter over 320 years. The diffusion rate taken is $\log D = -16.6\text{ m}^2\cdot\text{s}^{-1}$ – extrapolated from the fast oxidation related mechanism demonstrated by Reynes et al. 2018 for grossular at Servette peak temperature, $550\text{ }^\circ\text{C}$.

> 99% of initial water is diffused out after 300 years, and all sharp zonings are eliminated.